Provided for non-commercial research and education use.
Not for reproduction, distribution or commercial use.

This article appeared in a journal published by Elsevier. The attached copy is furnished to the author for internal non-commercial research and education use, including for instruction at the authors institution and sharing with colleagues.

Other uses, including reproduction and distribution, or selling or licensing copies, or posting to personal, institutional or third party websites are prohibited.

In most cases authors are permitted to post their version of the article (e.g. in Word or Tex form) to their personal website or institutional repository. Authors requiring further information regarding Elsevier's archiving and manuscript policies are encouraged to visit:

http://www.elsevier.com/copyright

Author's personal copy

Available online at www.sciencedirect.com
ScienceDirect
European Journal of Mechanics B/Fluids 27 (2008) 361–387

Numerical verification of the weak turbulent model for swell evolution

A.O. Korotkevich [a,*], A. Pushkarev [b,c], D. Resio [d], V.E. Zakharov [e,b,c,a]

[a] *Landau Institute for Theoretical Physics RAS, 2, Kosygin Str., Moscow, 119334, Russian Federation*
[b] *Lebedev Physical Institute RAS, 53, Leninsky Prosp., GSP-1 Moscow, 119991, Russian Federation*
[c] *Waves and Solitons LLC, 918 W. Windsong Dr., Phoenix, AZ 85045, USA*
[d] *Coastal and Hydraulics Laboratory, U.S. Army Engineer Research and Development Center, Halls Ferry Rd., Vicksburg, MS 39180, USA*
[e] *Department of Mathematics, University of Arizona, 617 N. Santa Rita Ave., Tucson, AZ 85721, USA*

Received 16 February 2007; received in revised form 17 August 2007; accepted 18 August 2007

Available online 28 August 2007

Abstract

The purpose of this article is to numerically verify the theory of weak turbulence. We have performed numerical simulations of an ensemble of nonlinearly interacting free gravity waves (a swell) by two different methods: by solving the primordial dynamical equations describing the potential flow of an ideal fluid with a free surface, and by solving the kinetic Hasselmann equation, describing the wave ensemble in the framework of the theory of weak turbulence. In both cases we have observed effects predicted by this theory: frequency downshift, angular spreading and formation of a Zakharov–Filonenko spectrum $I_\omega \sim \omega^{-4}$. To achieve quantitative coincidence of the results obtained by different methods, we have to augment the Hasselmann kinetic equation by an empirical dissipation term S_{diss} modeling the coherent effects of white-capping. Using the standard dissipation terms from the operational wave predicting model (*WAM*) leads to a significant improvement on short times, but does not resolve the discrepancy completely, leaving the question about the optimal choice of S_{diss} open. In the long run, *WAM* dissipative terms essentially overestimate dissipation.
© 2007 Elsevier Masson SAS. All rights reserved.

Keywords: Weak turbulence; Wave kinetic equation; Hasselmann equation; Numerical simulation

1. Introduction

The theory of weak turbulence is designed to statistically describe weakly nonlinear wave ensembles in dispersive media. The main tool of weak turbulence theory is the kinetic equation for squared wave amplitudes, or a system of such equations. Since the discovery of the kinetic equation for bosons by Nordheim [1] (see also the paper [2] by Peierls) in the context of solid state physics, this quantum-mechanical tool was applied to a wide variety of classical problems, including wave turbulence in hydrodynamics, plasmas, liquid helium, nonlinear optics, etc. (see monograph by Zakharov, Falkovich and Lvov [3]). Such kinetic equations have rich families of exact solutions describing weak-

* Corresponding author.
E-mail addresses: kao@itp.ac.ru (A.O. Korotkevich), andrei@cox.net (A. Pushkarev), zakharov@math.arizona.edu (V.E. Zakharov).

0997-7546/$ – see front matter © 2007 Elsevier Masson SAS. All rights reserved.
doi:10.1016/j.euromechflu.2007.08.004

Author's personal copy

turbulent Kolmogorov spectra. Also, kinetic equations for waves have self-similar solutions describing the temporal or spatial evolution of weak-turbulent spectra.

However, in our opinion, the most remarkable example of weak turbulence is a wind-driven sea. The kinetic equation statistically describing the gravity waves on the surface of ideal liquid was derived by Hasselmann [4]. Since this time, the Hasselmann equation has been widely used in physical oceanography as the foundation for developing wave-prediction models such as *WAM, SWAN* and *WAVEWATCH*. Among the other applications of the theory of weak turbulence, the Hasselmann equation stands out by virtue of its impact on industry.

In spite of the tremendous popularity of the Hasselmann equation, its validity and applicability for describing a real wind-driven sea has never been completely proven. It was criticized by many respected authors, not only in the context of oceanography. There are at least two reasons why the weak-turbulent theory could fail, or at least be incomplete.

The first reason is the presence of coherent structures. The weak-turbulent theory only describes weakly-nonlinear resonant processes. Such processes are spatially extended, they provide weak phase and amplitude correlation on distances significantly exceeding the wave length. However, nonlinearity also causes other phenomena, much more strongly localized in space. Such phenomena – solitons, quasi-solitons and wave collapses – are strongly nonlinear and cannot be described by the kinetic equations. Meanwhile, they may compete with weakly-nonlinear resonant processes and make comparable or even dominating contributions to the energy, momentum and wave-action balance. For gravity waves on the surface of a fluid, the most important coherent structures are white-cappings (or wave-breakings), which are essentially responsible for the dissipation of wave energy.

The second reason that limits the applicability of the weak-turbulent theory is the finite size of any real physical system. The kinetic equations are derived only for infinite media, where the wave vector runs along a continuous d-dimensional Fourier space. The situation is different for wave systems with boundaries, e.g. boxes with periodical or reflective boundary conditions. The Fourier space of such systems is an infinite lattice of discrete eigenmodes. If the spacing of the lattice is not small enough, or the level of Fourier modes is not large enough, the whole physics of nonlinear interaction becomes completely different from the continuous case. We shall call effects caused by a finite size of a system *mesoscopic effects*. These effects may be important in nature and they should certainly be taken into account when performing numerical simulations of wave turbulence.

For these two reasons, verifying the weak turbulent theory is an urgent problem, important for the whole physics of nonlinear waves. The verification can be performed by a direct numerical simulation of the primordial dynamical equations describing wave turbulence in a nonlinear medium.

So far, numerical experiments have been performed to check some predictions of the weak-turbulent theory, such as weak-turbulent Kolmogorov spectra. For gravity wave turbulence the most important is the Zakharov–Filonenko spectrum $F_\omega \sim \omega^{-4}$ [5]. This spectrum has already been observed in numerous numerical experiments [6–20]. Attempts at verifying weak turbulent theory through numerical simulation of the primordial dynamical equations have been started with a numerical simulation of 2D optical turbulence [21], which demonstrated, in particular, the co-existence of weak-turbulent and coherent events.

A numerical simulation of 2D-turbulence of capillary waves was performed in [6–8]. The main results of the simulation consisted in observing the classical regime of weak turbulence with the spectrum $F_\omega \sim \omega^{-19/4}$, and the discovery of a non-classical regime of so-called *frozen turbulence*, characterized by an absence of energy transfer from low to high wave-numbers. The classical regime of turbulence was observed on a grid of 256×256 points at relatively high levels of excitation, while the frozen regime was realized at lower levels of excitation, or more coarse grids. The effect of frozen turbulence is explained by mesoscopic effects: sparsity of both exact and approximate resonances. The classical regime of turbulence becomes possible due to a broadening of resonances by nonlinearity. The classical and the frozen regime can coexist. We call this situation *mesoscopic turbulence*.

In fact, the frozen turbulence is close to a *KAM* regime, when the dynamics of turbulence is close to the behavior of an integrable system [8].

Simulations of surface gravity waves turbulence were first done simultaneously by Tanaka [9] and Onorato at al. [10]. Due to the computational limitations of computers of the time, the simulations were limited to dynamical equations and fairly short simulation times. Many articles later developed these pioneering results [11–17]. Nonlinear effects for gravity waves are weaker than for capillary waves; as a result, the influence of mesoscopic effects is stronger. This makes the simulations much more difficult. In the experiments mentioned above, the grid was fine enough to resolve the spectral tails and observe the weak turbulent Kolmogorov asymptotics $I_k \sim k^{-4}$, but it was too coarse to avoid mesoscopic effects in the area of the spectral peak. The finest grid 2048×4096 was used by Tanaka,

Author's personal copy

however, in his experiments the spectral peak was posed at $k = 68$, while the level of nonlinearity was quite small (typical steepness $\mu \simeq 0.07$). Moreover, his experiment was very short in terms of characteristic wave time (only several tens periods of the leading wave). Had he continued his calculations, he would have observed the formation of the weak turbulent Kolmogorov tail as in the work by Onorato at al. [10]. However, his spectral peak was seriously distorted by mesoscopic effects.

In this article, we present the results of a simulation of surface gravity wave turbulence, namely, we model swell propagation. All previous researchers since Tanaka [9] and Onorato at al. [10] performed only one type of experiment – solution of the primordial dynamical equations. We performed two experiments simultaneously. We solved not only the dynamical equations but also the Hasselmann kinetic equation and compared the results. We think that our results can be considered as the first attempt to directly verify the Hasselmann kinetic equation.

In the dynamic experiment, we used a coarser grid than Tanaka (512×4096) but we posed the spectral peak at $k = 300$, and our initial steepness was much higher than in Tanaka's case ($\mu \simeq 0.15$). Due to much higher k and stronger nonlinearity we basically managed to suppress mesoscopic effects. According to the weak-turbulent scenario, the bulk of energy containing modes satisfies the Rayleigh distribution. The distribution has a heavy tail of abnormally intensive harmonics (*oligarchs*, according to the terminology introduced in the article [15]), but they contain no more than 5% of total energy.

One important point should be mentioned. In our experiments we not only observed weak turbulence, but also additional nonlinear dissipation of the wave energy, which may be identified as the dissipation due to white-capping. We observed a rapid broadening of the spectra due to multiple harmonics generation. The formation of a broad spectrum with strong small scale tails can be explained by the formation of rather sharp structures on wave crests. Further development of these tails is suppressed by an artificial dissipation used in our dynamical experiment. One can say that in such a way we roughly simulated the phenomenon of white-capping (continuous in time dissipation of energy due to multiple acts of wave braking on the very edge of wave crest, arresting formation of derivative singularities on the sharp wave crest). Of course, we cannot directly simulate wave breaking, but our method may provide a rough but reasonable simulation of this effect.

To reach agreement with dynamic experiments, we had to add to the kinetic equation a phenomenological dissipation term S_{diss}. In this article we examined the dissipation terms used in the operational wave-prediction models *WAM cycle 3* and *WAM cycle 4* (hereafter referred to as *WAM3* and *WAM4* correspondingly). Both of these terms significantly overestimate nonlinear dissipation. The term given in *WAM3* gives acceptable results for short periods of time (less than $1000T_0$, where T_0 is the time period of the leading wave of the initial condition). But at the end of simulation ($t = 3378T_0$) the error in wave action approached 30%. For *WAM4* the situation is even worse. If the characteristic wave length of the initial conditions is equal to 22 m, then $3378T_0$ is only slightly more than 3 hours of wave development. Even a primitive viscous dissipative term without any simulation of strongly nonlinear events gives us better results. This means that the question about a reasonable formula for S_{diss} remains open.

2. Deterministic and statistic models

In the dynamical part of our experiment, the surface of the fluid is described by two functions of horizontal variables x, y and time t: the surface elevation $\eta(x, y, t)$ and the velocity potential on the surface $\psi(x, y, t)$. They satisfy the canonical equations [24]

$$\frac{\partial \eta}{\partial t} = \frac{\delta H}{\delta \psi}, \qquad \frac{\partial \psi}{\partial t} = -\frac{\delta H}{\delta \eta}. \tag{1}$$

The Hamiltonian H is given by the first three terms in the power expansion on the nonlinearity $\nabla\eta$

$$\begin{aligned}
H &= H_0 + H_1 + H_2 + \cdots,\\
H_0 &= \frac{1}{2}\int (g\eta^2 + \psi\hat{k}\psi)\,\mathrm{d}x\,\mathrm{d}y,\\
H_1 &= \frac{1}{2}\int \eta\big[|\nabla\psi|^2 - (\hat{k}\psi)^2\big]\,\mathrm{d}x\,\mathrm{d}y,\\
H_2 &= \frac{1}{2}\int \eta(\hat{k}\psi)\big[\hat{k}\big(\eta(\hat{k}\psi)\big) + \eta\nabla^2\psi\big]\,\mathrm{d}x\,\mathrm{d}y.
\end{aligned} \tag{2}$$

Author's personal copy

Here $\hat{k}$ is the linear integral operator $\hat{k} = \sqrt{-\nabla^2}$, defined in Fourier space as

$$\hat{k}\psi_{\vec{r}} = \frac{1}{2\pi}\int |k|\psi_{\vec{k}} \mathrm{e}^{-\mathrm{i}\vec{k}\vec{r}}\,\mathrm{d}\vec{k}, \quad |k| = \sqrt{k_x^2 + k_y^2}. \tag{3}$$

Using the Hamiltonian (2) and Eqs. (1) we obtain the dynamical equations [6]:

$$\begin{aligned}
\dot{\eta} &= \hat{k}\psi - \big(\nabla(\eta\nabla\psi)\big) - \hat{k}[\eta\hat{k}\psi] + \hat{k}\big(\eta\hat{k}[\eta\hat{k}\psi]\big) + \frac{1}{2}\nabla^2[\eta^2\hat{k}\psi] + \frac{1}{2}\hat{k}[\eta^2\nabla^2\psi] + \hat{F}^{-1}[\gamma_k\eta_k],\\
\dot{\psi} &= -g\eta - \frac{1}{2}\big[(\nabla\psi)^2 - (\hat{k}\psi)^2\big] - [\hat{k}\psi]\hat{k}[\eta\hat{k}\psi] - [\eta\hat{k}\psi]\nabla^2\psi + \hat{F}^{-1}[\gamma_k\psi_k].
\end{aligned} \tag{4}$$

Here $\hat{F}^{-1}$ corresponds to the inverse Fourier transform. We introduced artificial dissipative terms $\hat{F}^{-1}[\gamma_k\eta_k]$ and $\hat{F}^{-1}[\gamma_k\psi_k]$, corresponding to pseudo-viscous high frequency damping, following the recent work [19].

The model (1)–(4) was used in the numerical experiments [6–8,12,13,15,17,18].

We introduce the complex normal variables $a_{\vec{k}}$

$$a_{\vec{k}} = \sqrt{\frac{\omega_k}{2k}}\eta_{\vec{k}} + \mathrm{i}\sqrt{\frac{k}{2\omega_k}}\psi_{\vec{k}}, \tag{5}$$

where $\omega_k = \sqrt{gk}$, to transform Eqs. (1) into

$$\frac{\partial a_{\vec{k}}}{\partial t} = -\mathrm{i}\frac{\delta H}{\delta a_{\vec{k}}^*}. \tag{6}$$

To proceed with the statistical description of the wave ensemble, we first need to perform the canonical transformation $a_{\vec{k}} \to b_{\vec{k}}$, which excludes the cubical terms in the Hamiltonian. The details of this transformation can be found in the paper (1999) [25] by Zakharov. After the transformation, the Hamiltonian takes the form

$$H = \int \omega_{\vec{k}} b_{\vec{k}} b_{\vec{k}}^*\,\mathrm{d}\vec{k} + \frac{1}{4}\int T_{\vec{k}\vec{k}_1\vec{k}_2\vec{k}_3} b_{\vec{k}}^* b_{\vec{k}_1}^* b_{\vec{k}_2} b_{\vec{k}_3}\delta_{\vec{k}+\vec{k}_1-\vec{k}_2-\vec{k}_3}\,\mathrm{d}\vec{k}_1\,\mathrm{d}\vec{k}_2\,\mathrm{d}\vec{k}_3, \tag{7}$$

where T is a homogeneous function of third order:

$$T(\varepsilon\vec{k}, \varepsilon\vec{k}_1, \varepsilon\vec{k}_2, \varepsilon\vec{k}_3) = \varepsilon^3 T(\vec{k}, \vec{k}_1, \vec{k}_2, \vec{k}_3). \tag{8}$$

The relation between $a_{\vec{k}}$ and $b_{\vec{k}}$, together with an explicit expression for $T_{\vec{k}\vec{k}_1\vec{k}_2\vec{k}_3}$ can be found, for example, in [25].

Introduce the pair correlation function

$$\langle a_{\vec{k}} a_{\vec{k}'}^* \rangle = g N_{\vec{k}}\delta(\vec{k} - \vec{k}'), \tag{9}$$

where $N_{\vec{k}}$ is the spectral density of the wave function. This definition of the wave action is common in oceanography.

We also introduce the correlation function for transformed normal variables

$$\langle b_{\vec{k}} b_{\vec{k}'}^* \rangle = g n_{\vec{k}}\delta(\vec{k} - \vec{k}'). \tag{10}$$

The functions $n_{\vec{k}}$ and $N_{\vec{k}}$ can be expressed in terms of each other by cumbersome power series [25] of expansion on μ, where μ is the characteristic steepness, defined as follows:

$$\mu = \frac{E^2}{N^2}\sqrt{2E}, \tag{11}$$

where E is the wave energy and N is the wave action. Following this definition, for a Stokes wave of small amplitude

$$\begin{aligned}
&\eta = a\cos(kx),\\
&\mu \simeq ak.
\end{aligned}$$

On deep water, the relative difference between $n_{\vec{k}}$ and $N_{\vec{k}}$ is of the order of μ^2 and can be neglected (in most cases, experimental results give $\mu \simeq 0.1$).

Author's personal copy

The spectrum $n_{\vec{k}}$ satisfies the Hasselmann (kinetic) equation [4]

$$\frac{\partial n_{\vec{k}}}{\partial t} = S_{\mathrm{nl}}[n] + S_{\mathrm{diss}} + 2\gamma_k n_{\vec{k}},$$
$$S_{\mathrm{nl}}[n] = 2\pi g^2 \int |T_{\vec{k},\vec{k}_1,\vec{k}_2,\vec{k}_3}|^2 (n_{\vec{k}_1} n_{\vec{k}_2} n_{\vec{k}_3} + n_{\vec{k}} n_{\vec{k}_2} n_{\vec{k}_3} - n_{\vec{k}} n_{\vec{k}_1} n_{\vec{k}_2} - n_{\vec{k}} n_{\vec{k}_1} n_{\vec{k}_3}) \delta(\omega_k + \omega_{k_1} - \omega_{k_2} - \omega_{k_3})$$
$$\times \delta(\vec{k} + \vec{k}_1 - \vec{k}_2 - \vec{k}_3)\, \mathrm{d}\vec{k}_1\, \mathrm{d}\vec{k}_2\, \mathrm{d}\vec{k}_3. \tag{12}$$

Here S_{diss} is an empirical dissipation term that corresponds to white-capping.

The stationary conservative kinetic equation

$$S_{\mathrm{nl}} = 0 \tag{13}$$

has a rich family of Kolmogorov-type [26] exact solutions. Among them is the Zakharov–Filonenko spectrum [5] for the direct cascade of energy

$$n_k \sim \frac{1}{k^4}, \tag{14}$$

and the Zakharov–Zaslavskii [27,28] spectra for the inverse cascade of wave action

$$n_k \sim \frac{1}{k^{23/6}}. \tag{15}$$

3. Deterministic numerical experiment

3.1. Setup of the problem

The dynamical equations (4) are solved in the real-space domain $2\pi \times 2\pi$ on a 512×4096 grid with the gravity acceleration set to $g = 1$. The solution has been performed by the spectral code developed in [22] and previously used in [23,12,13,15]. We stress that in the current computations the resolution in the Y-direction (long axis) is better than the resolution in the X-direction by a factor of 8.

This approach is reasonable if the swell is essentially anisotropic, almost one-dimensional. This assumption will be validated by a proper choice of the initial data for computation. As the initial condition, we used a Gaussian-shaped distribution in Fourier space (see Fig. 1):

$$\begin{cases} |a_{\vec{k}}| = A_i \exp\left(-\frac{1}{2}\frac{|\vec{k}-\vec{k}_0|^2}{D_i^2}\right), & |\vec{k}-\vec{k}_0| \leqslant 2D_i, \\ |a_{\vec{k}}| = 10^{-12}, & |\vec{k}-\vec{k}_0| > 2D_i, \end{cases}$$
$$A_i = 0.92 \times 10^{-6}, \qquad D_i = 60,$$
$$\vec{k}_0 = (0; 300), \qquad \omega_0 = \sqrt{g k_0}. \tag{16}$$

The initial phases of all harmonics are random. The average steepness of this initial condition is $\mu \simeq 0.15$ (defined in accordance with Eq. (11)).

To realize a similar experiment in a laboratory wave tank, it would be required to generate the waves with wavelength 300 times less than the length of the tank. The width of the tank would have to be no less than $1/8$ of its length. The minimal wave length of the gravitational wave in the absence of capillary effects can be estimated as $\lambda_{\min} \simeq 3$ cm. The leading wavelength is be an order of magnitude larger: $\lambda \simeq 30$ cm.

In such a large tank, 200×25 meters in dimension, experimenters can observe the evolution of the swell until approximately $700T_0$ – still less than in our experiments. In tanks of smaller size, the effects of discreetness in the Fourier space dominate, and either frozen or mesoscopic wave turbulence will be observed, qualitatively different from the wave turbulence in the ocean.

To stabilize high-frequency numerical instability, the damping function has been chosen as

$$\gamma_k = \begin{cases} 0, & k < k_d, \\ -\gamma(k-k_d)^2, & k \geqslant k_d, \end{cases}$$
$$k_d = 1024, \qquad \gamma = 5.65 \times 10^{-3}. \tag{17}$$

Author's personal copy

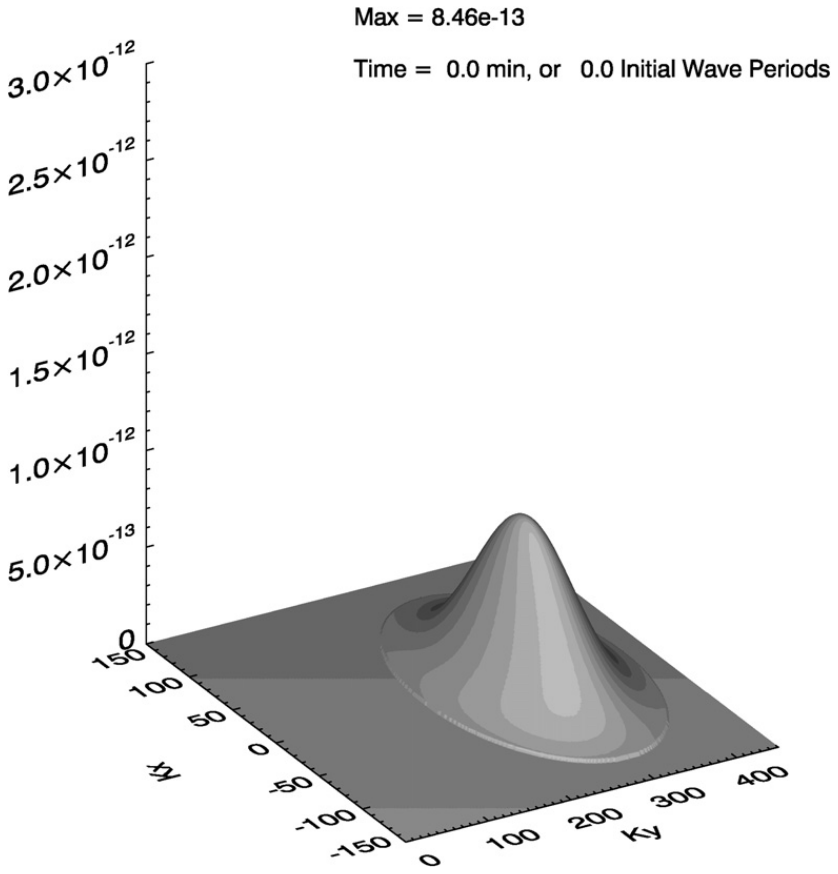

Fig. 1. The initial distribution of $|a_{\vec{k}}|^2$ on $\vec{k}$-plane.

The simulation was performed until $t = 1225$, which is equivalent to $3378T_0$, where $T_0 = 2\pi/\sqrt{k_0}$ is the period of the wave, corresponding to the maximum of the initial spectral distribution.

3.2. Zakharov–Filonenko spectra

As in the previous papers [10,12,13,15], we observed the rapid formation of the spectral tail, described by Zakharov–Filonenko law for the direct cascade $n_k \sim k^{-4}$ [5] (see Fig. 2). In agreement with [15], the spectral maximum slowly downshifts to the large-scale region, which corresponds to the inverse cascade [27,28].

We also directly measured the energy spectrum during the final stage of the simulation, when the spectral downshift was sufficiently slow. This experiment can be interpreted as an ocean buoy record – we recorded the time series of the surface elevation at one point of the surface during $T_{\text{buoy}} \simeq 300T_0$. The Fourier transform of the autocorrelation function

$$E(\omega) = \frac{1}{2\pi} \int_{-T_{\text{buoy}}/2}^{T_{\text{buoy}}/2} \langle \eta(t+\tau)\eta(\tau) \rangle e^{i\omega t}\, d\tau\, dt. \tag{18}$$

allows us to detect the direct cascade spectrum tail proportional to ω^{-4} (see Fig. 3), well-known from experimental observations [29–31].

In this paper we had no intention of improving the results of the previous papers. The inertial interval of the angle-averaged spectra (the ω-spectrum is also angle-averaged because it depends only on the frequency $\omega \sim \sqrt{k}$) is limited due to the anisotropy of the integration domain. In this case we have less than one decade interval and we cannot securely detect an exponent of the Kolmogorov tail, however, this work has already been done in several previous articles (see, for instance, [13]). Here we limit our observations to qualitative correspondence.

Author's personal copy

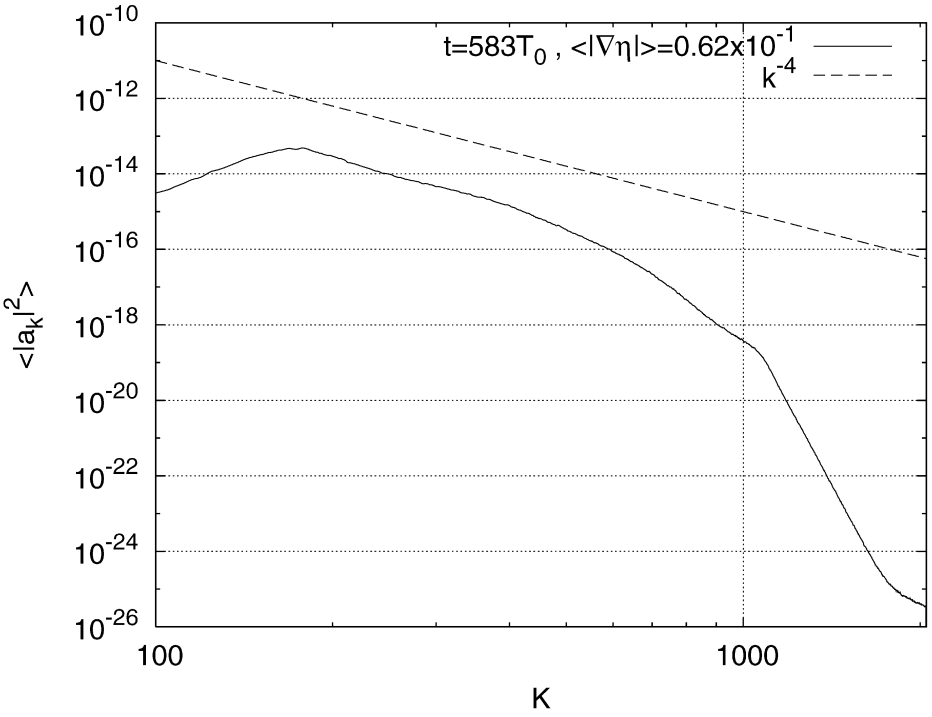

Fig. 2. Angle-averaged spectrum $n_k = \langle |a_{\vec{k}}|^2 \rangle$ in a double logarithmic scale. The tail of distribution fits the Zakharov–Filonenko spectrum.

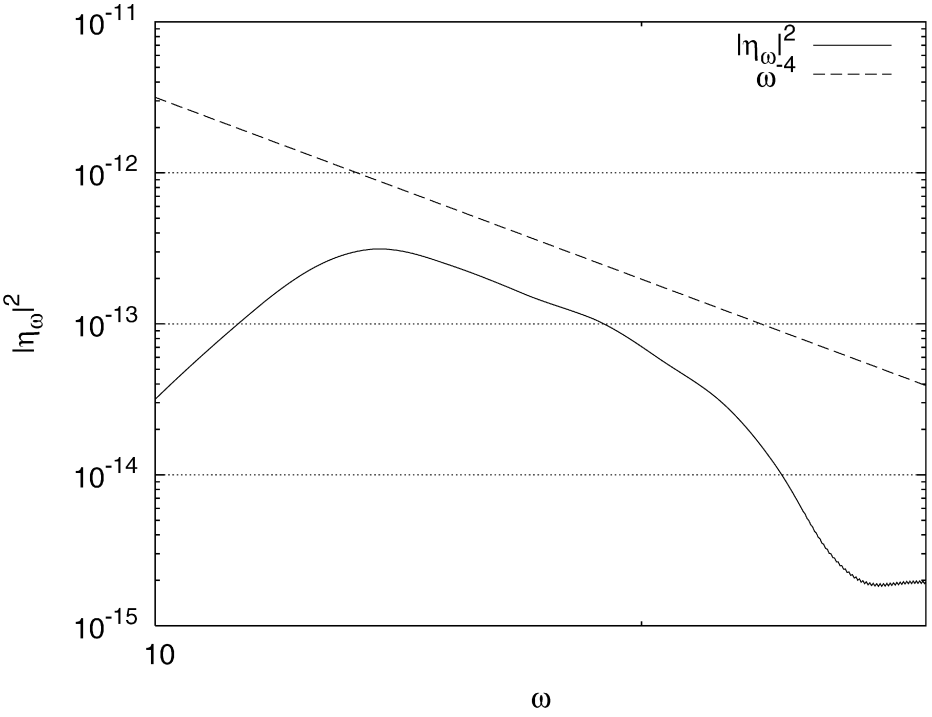

Fig. 3. The energy spectrum in a double logarithmic scale. The distribution tail fits to the asymptotic ω^{-4}.

3.3. Is the weak-turbulent scenario realized?

The presence of the Kolmogorov asymptotic in spectral tails, however, is not enough to validate the applicability of the weak-turbulent scenario to the description of the wave ensemble. We also have be sure that the statistical properties of the ensemble correspond to the assumptions of the weak-turbulent theory.

Author's personal copy

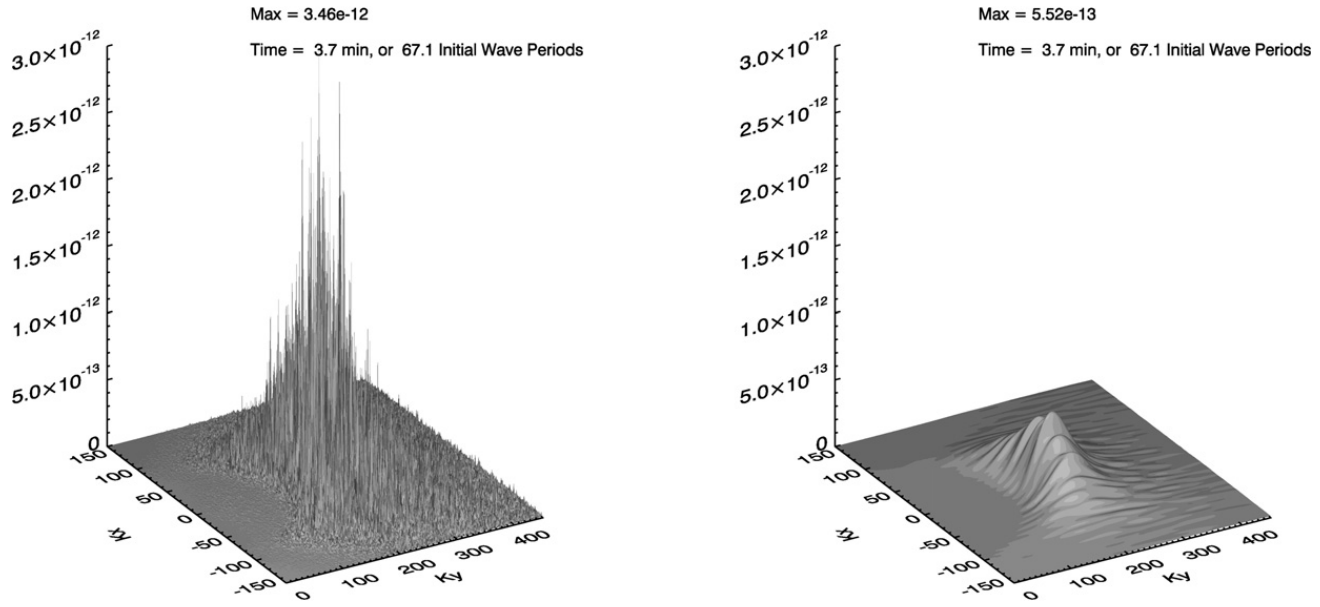

Fig. 4. The surface $|a_{\vec{k}}|^2$ before (left) and after (right) a low-pass filter at the moment of time $t \simeq 67T_0$.

We stress that at the beginning of our experiments, $|a_{\vec{k}}|^2$ is a smooth function of $\vec{k}$. Only the phases of the individual waves are random. As the numerical simulation shows, the initial condition (16) (see Fig. 1) does not preserve its smoothness – it becomes rough virtually immediately (see Fig. 4). The picture of this roughness is remarkably preserved in many details, even as the spectrum down-shifts as a whole. This roughness does not contradict the weak-turbulent theory. According to this theory, the wave ensemble is almost Gaussian, and both the real and the imaginary parts of each separate harmonic are non-correlated. However, also according to the weak-turbulent theory, the spectra must become smooth after averaging over a sufficient period of time, greater than $1/\mu^2$ periods. Earlier, we observed such a restoration of smoothness in the numerical experiments of the *MMT* model (see [47–50]). However, in the experiments discussed in the article, the roughness persists and the averaging does not suppress it completely. This can be explained by the sparsity of the resonances.

The conditions of resonance are defined by the system

$$\begin{aligned} &\omega_k + \omega_{k_1} = \omega_{k_2} + \omega_{k_3}, \\ &\vec{k} + \vec{k}_1 = \vec{k}_2 + \vec{k}_3. \end{aligned} \tag{19}$$

These conditions define a five-dimensional hypersurface in six-dimensional space $\vec{k}, \vec{k}_1, \vec{k}_2$. In a finite system, (19) becomes a Diophantine equation. Some solutions of this equation are known [32,17]. In reality, however, energy transport is realized by approximate, rather that exact, resonances, posed in a layer near the resonant surface and defined by

$$|\omega_k + \omega_{k_1} - \omega_{k_2} - \omega_{k+k_1-k_2}| \leqslant \Gamma, \tag{20}$$

where Γ is a characteristic inverse time of nonlinear interaction.

In finite systems, $\vec{k}, \vec{k}_1, \vec{k}_2$ take values on the nodes of a discrete grid. The weak turbulent approach is valid if the density of discrete approximate resonances inside the layer (20) is high enough. In our case the lattice constant is $\Delta k = 1$, and the typical relative deviation from the resonance surface is

$$\frac{\Delta\omega}{\omega} \simeq \frac{\omega'_k}{\omega}\Delta k = \frac{\omega'_k}{\omega} \simeq \frac{1}{600} \simeq 2 \times 10^{-3}. \tag{21}$$

The inverse interaction time Γ can be estimated from our numerical experiments: wave amplitudes change essentially during 30 periods, and we can assume that $\Gamma/\omega \simeq 10^{-2} \gg \frac{\delta\omega}{\omega}$. This means that the applicability condition of the weak turbulent theory is typically satisfied, but the reserve for its validity is rather modest. As a result, some particular harmonics, posed in certain privileged points of the k-plane may form a network of almost resonant quadruples and be responsible for a significant part of energy transport. The amplitudes of these harmonics essentially exceed the

Author's personal copy

average level. This effect was described in the article [15], where these few selected harmonics were called *oligarchs*. If the *oligarchs* are responsible for the greater part of the energy flux, the turbulence is mesoscopic, rather than weak.

3.4. Statistics of the harmonics

According to the weak-turbulent scenario, the statistics of the $a_{\vec{k}}(t)$ in any given $\vec{k}$ should be close to Gaussian. This presumes that the PDF for the squared amplitudes is

$$P\left(|a_{\vec{k}}|^2\right) \simeq \frac{1}{D} \mathrm{e}^{-|a_{\vec{k}}|^2/D}, \tag{22}$$

where $D = \langle |a_{\vec{k}}|^2 \rangle$ is the mean square amplitude.

To check Eq. (22), we need to find a way to calculate $D(\vec{k})$. If the ensemble is stationary in time, $D(\vec{k})$ can be found for any given $\vec{k}$ by averaging over time. In our case, the process is non-stationary, and we have a problem with determining $D(\vec{k})$.

To resolve this problem, we used low-pass filtering instead of time averaging. The low-pass filter was taken in the form

$$\begin{aligned} &f(\vec{n}) = \mathrm{e}^{-(|\vec{n}|/\Delta)^3}, \\ &\Delta = 0.25 \cdot N_x/2, \quad N_x = 4096, \end{aligned} \tag{23}$$

where $\vec{n}$ is an integer vector running along K-space.

This choice of low-pass filter preserves the values of total energy, wave action and the total momentum within three percent accuracy. The shape of low-pass filtered function is given on Fig. 4. It is now possible to average the PDF over different areas of k-space. The results for two different moments of time $t \simeq 67.1T_0$ and $t \simeq 925T_0$ are shown in Fig. 5 and Fig. 6. The thin line gives the PDF after averaging over dissipation region harmonics, while the bold line gives averaging over the non-dissipative area $|\vec{k}| < k_d = 1024$. We can see that the statistics in the last case is quite close to the Gaussian, while in the dissipation region it deviates from the Gaussian distribution. However, deviation from the Gaussian in the dissipation region does not create any problems, since the dissipative harmonics do not contain any essential amount of the total energy, wave action and momentum.

We stress that the bold lines in Figs. 5 and 6 are the results of averaging over a million harmonics. Among them there is a population of selected few, or *oligarchs*, with amplitudes exceeding the average value by a factor of more than ten. The oligarchs exist because our grid is still not fine enough. The contribution of such oligarchs in our case to the total wave action does not exceed 4%.

3.5. Two-stage evolution of the swell

Figs. 7–10 demonstrate the time evolution of the main characteristics of the wave field: wave action, energy, characteristic slope and mean frequency.

We specially comment Fig. 9. Here and further, we define the characteristic slope as defined in Eq. (11). According to this definition of steepness, for the classical Pierson–Moscowitz spectrum $\mu = 0.095$. Our initial steepness $\mu \simeq 0.15$ essentially exceeds this value.

The observed evolution of the spectrum can be conventionally separated into two phases. In the first stage, we observe a rapid drop of wave action, slope and especially energy. The drop then stabilizes, and we observe a slow downshift of mean frequency together with angular spreading. The level lines of smoothed spectra in the first and in the last moments of time are shown in Figs. 11–12.

The two stages can be understood through the study of the Probability Distribution Functions (PDFs) of the elevations of the surface. In all figures, we compare the distribution in experimental results with Gaussian distribution and Tayfun distribution [33]. The latter case is just a first correction to Gaussian distribution due to small nonlinearity. We use an explicit form of Tayfun distribution following [16]. In the initial moment of time, the PDF is Gaussian (see Fig. 13). No nonlinear interaction is involved, so the Tayfun distribution does not fit at all. However, very soon intensive super-Gaussian tails appear (see Fig. 14). They are well described by the Tayfun distribution. The tails then decrease slowly (Fig. 15), and in the last moment of the simulation, when the characteristics of the sea are close to

Author's personal copy

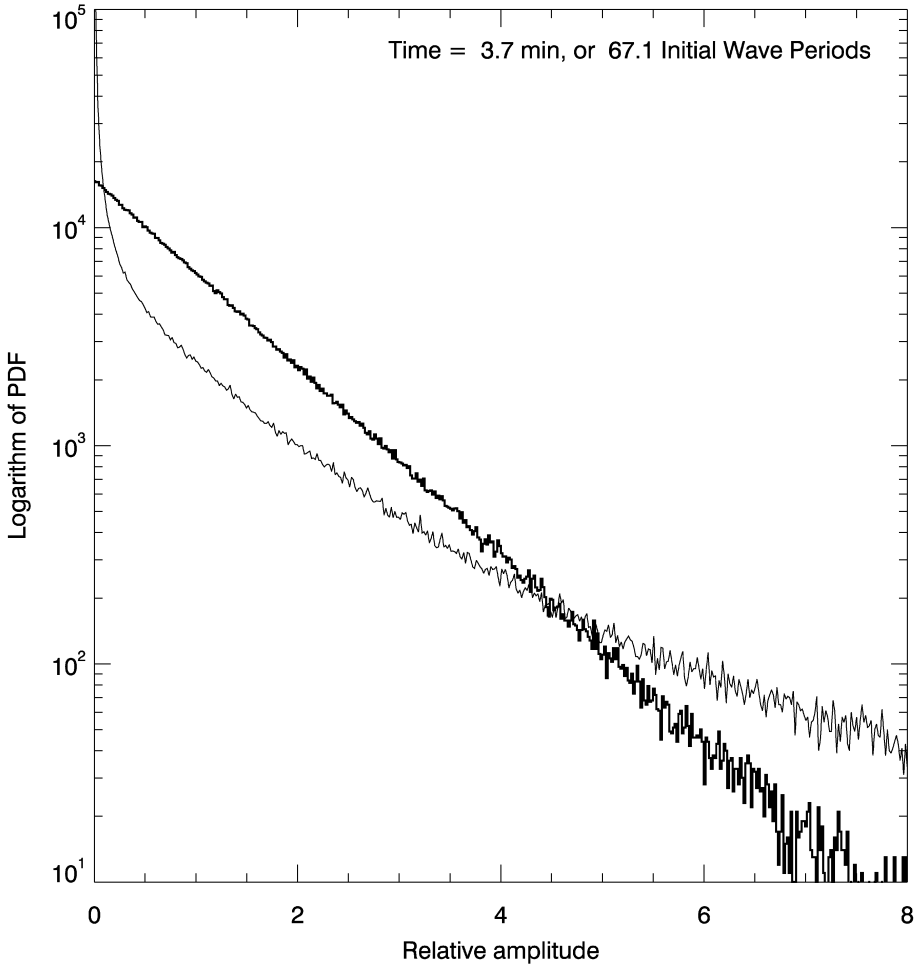

Fig. 5. The probability distribution function for the relative squared amplitudes $|a_k|^2/\langle|a_k|^2\rangle$. $t \simeq 67T_0$. The thin and bold lines correspond to averaging over dissipation and dissipation-free regions of $\vec{K}$-space, correspondingly.

Peirson–Moscowitz, the statistics is close to Gaussian again (Fig. 16). Moderate tails do exist and, in good agreement with Tayfun correction, troughs are more probable than crests which, in turn, can be much larger in absolute value. PDF for η_y – the longitudinal gradients in the first moment of time is Gaussian (Fig. 17). Then, in a very short period of time, strong non-Gaussian tails appear and reach their maximum at $t \simeq 14T_0$ (Fig. 18). Here $T_0 = 2\pi/\sqrt{k_0}$ is period of initial leading wave. After this moment the non-Gaussian tails decrease. In the last moment of simulation they are essentially reduced (Fig. 19).

The rapid growth of non-Gaussian tails can be explained by the formation of coherent harmonics. Indeed, $14T_0 \simeq 2\pi/(\omega_0\mu)$ is a characteristic time of nonlinear processes due to quadratic nonlinearity. Note that the fourth harmonic in our system is strongly decaying, hence we cannot see real white caps.

Figs. 20–22 show PDFs for the gradients in the orthogonal direction.

Figs. 23, 24 are snapshots of the surface in the initial and final moments of simulation. Fig. 25 is a snapshot of the surface in the moment of maximal roughness $T = 4.94 \simeq 14T_0$.

4. Statistical numerical experiment

4.1. A numerical model for the Hasselmann equation

The numerical integration of the kinetic equation for gravity waves on deep water (the Hasselmann equation) was the subject of considerable efforts over the last three decades. The ultimate goal of the effort was the creation of an operational wave model for wave forecasting based on a direct solution of the Hasselmann equation. This happened

Author's personal copy

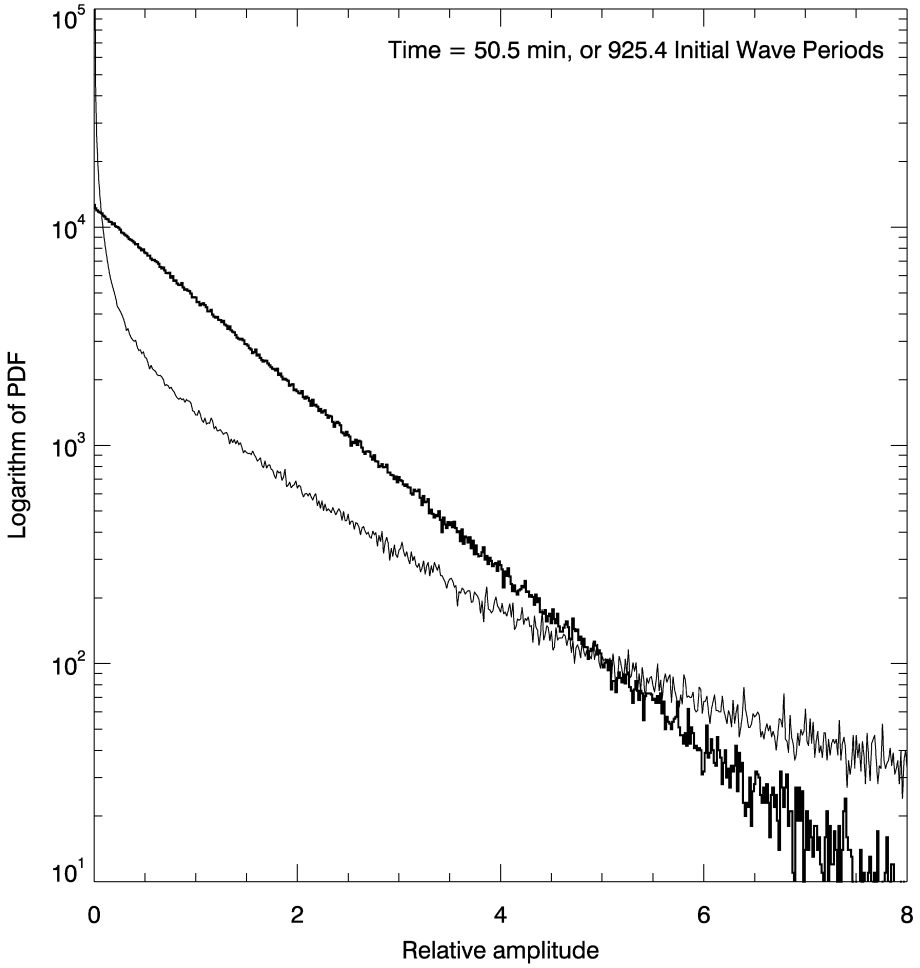

Fig. 6. The probability distribution function for relative squared amplitudes $|a_k|^2/\langle|a_k|^2\rangle$. $t \simeq 925T_0$. The thin and bold lines correspond to, averaging over dissipation and dissipation-free regions of $\vec{K}$-space correspondingly.

to be an extremely difficult computational problem due to mathematical complexity of the S_{nl} term, which requires calculating a three-dimensional integral at every moment of time.

Historically, numerical methods of integrating the kinetic equation for gravity waves come in two flavors.

The first one is associated with the works [34–39], and is based on transforming the 6-fold into 3-fold integrals using δ-functions. Such transformations lead to the appearance integrable singularities, which creates additional difficulties in calculating the S_{nl} term.

The second type of model was developed in [40–42] and is currently known as the Resio–Tracy model. It uses direct calculation of resonant quadruplet contribution into S_{nl} integral, based on the following property: given two fixed vectors $\vec{k}, \vec{k}_1$, another two $\vec{k}_2, \vec{k}_3$ are uniquely defined by the point moving along the resonant curve – the locus.

The numerical simulation in the present work was performed using a modified version of the second type algorithm. Calculations were made on a 71×36 grid in the frequency-angle domain $[\omega, \theta]$ with exponential distribution of points in the frequency domain and uniform distribution of points in the angle direction.

To date, Resio–Tracy model has undergone rigorous testing and is currently considered to have a high degree of trustworthiness. It has been tested with respect to motion integrals conservation in "clean" tests, wave action conservation in wave spectrum down-shift, realization of self-similar solution in pure swell and wind-forced regimes (see [44,43,45]).

We give a description of scaling procedures from dynamical equations to Hasselmann kinetic equation variables in Appendix A.

Author's personal copy

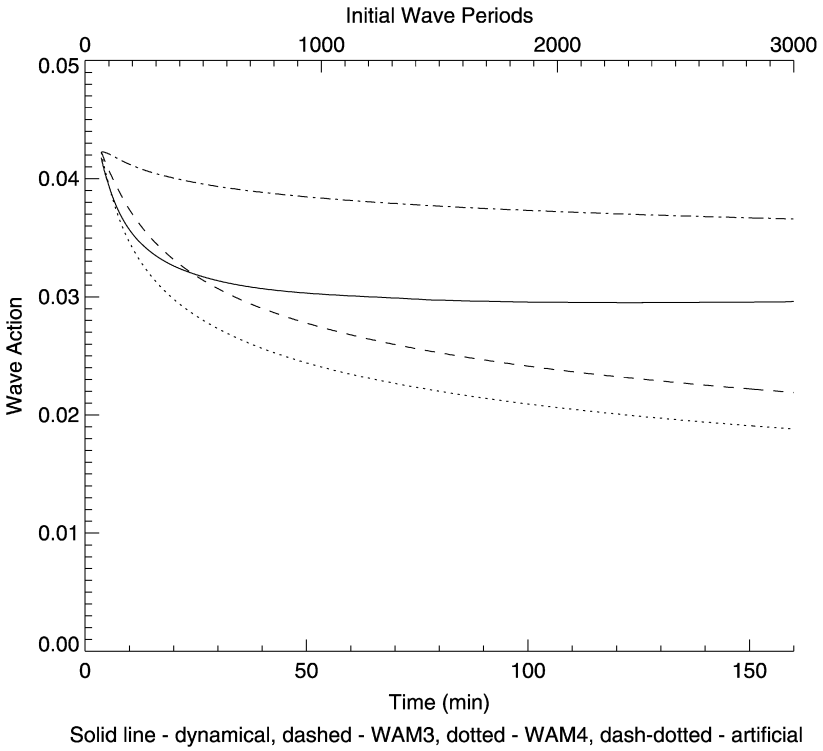

Fig. 7. Total wave action as a function of time. The solid line corresponds to the dynamical equations, dashed–dotted line – to the kinetic equation with artificial viscosity, dashed line – to the kinetic equation with a *WAM3* damping term, dotted line – to the kinetic equation with a *WAM4* damping term.

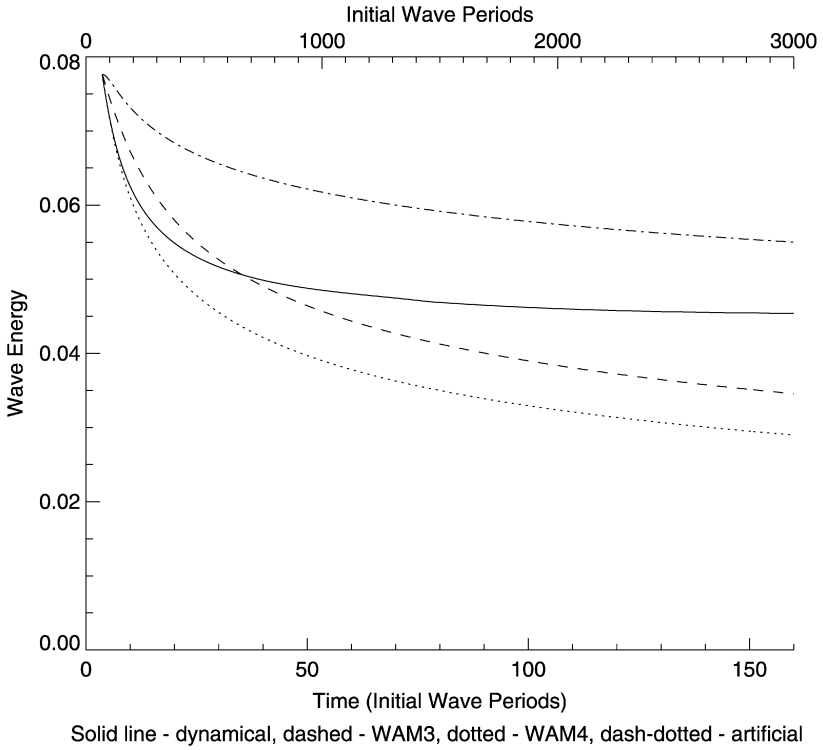

Fig. 8. Total wave energy as a function of time. The solid line corresponds to the dynamical equations, dashed–dotted line – to the kinetic equation with artificial viscosity, dashed line – to the kinetic equation with a *WAM3* damping term, dotted line – to the kinetic equation with a *WAM4* damping term.

Author's personal copy

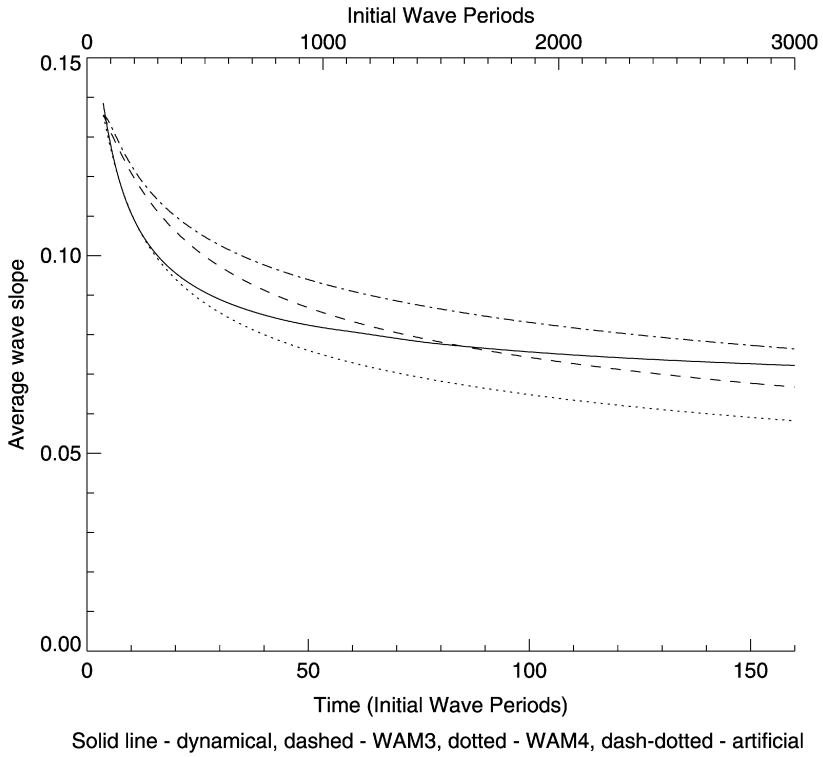

Fig. 9. Average wave slope as a function of time. The solid line corresponds to the dynamical equations, dashed–dotted line – to the kinetic equation with artificial viscosity, dashed line – to the kinetic equation with a *WAM3* damping term, dotted line – to the kinetic equation with a *WAM4* damping term.

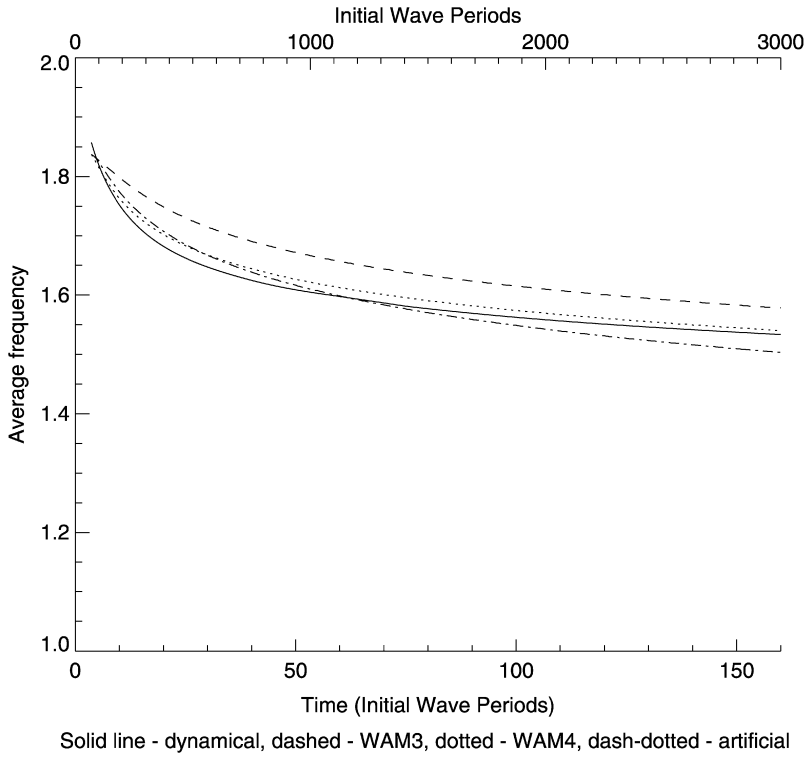

Fig. 10. Mean wave frequency as a function of time. The solid line corresponds to the dynamical equations, dashed–dotted line – to the kinetic equation with artificial viscosity, dashed line – to the kinetic equation with a *WAM3* damping term, dotted line – to the kinetic equation with a *WAM4* damping term.

Author's personal copy

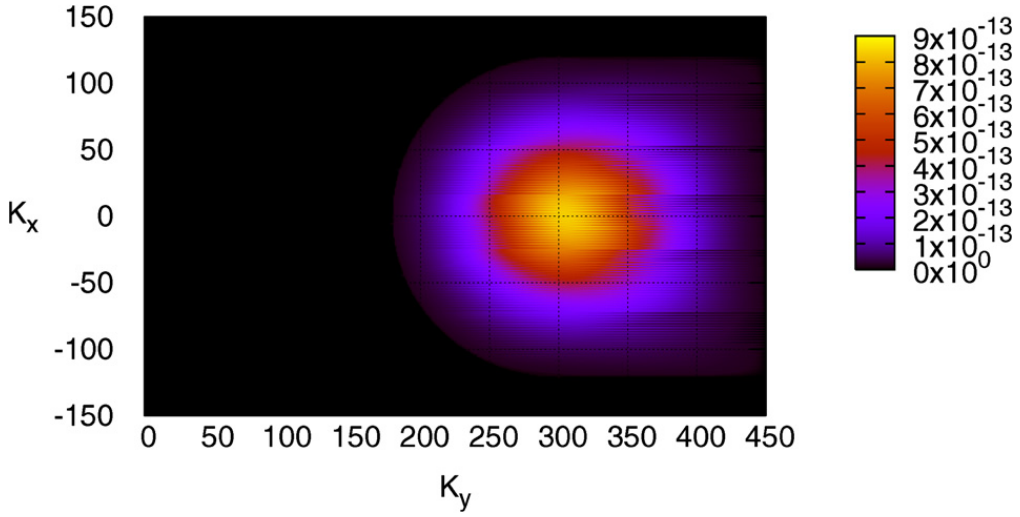

Fig. 11. Initial spectrum $|a_{\vec{k}}|^2$. $t = 0$.

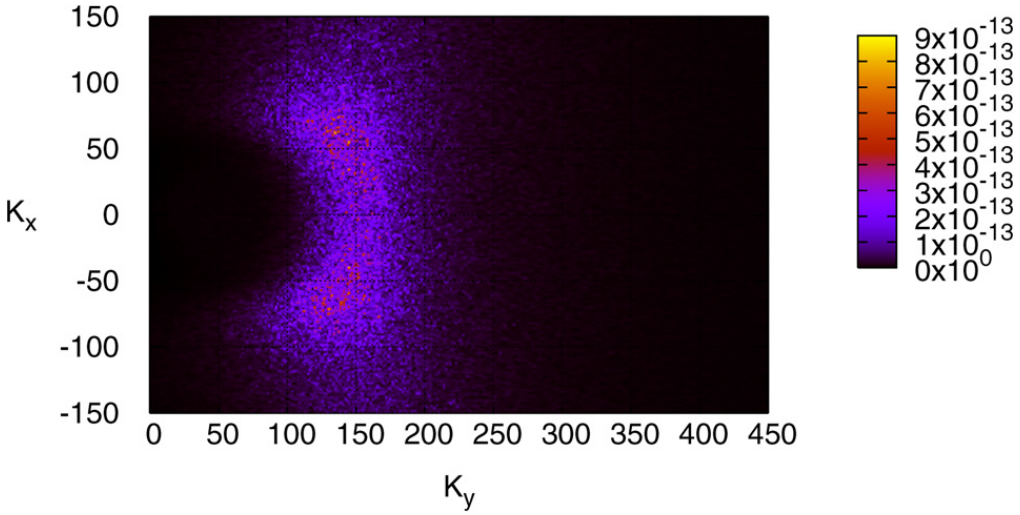

Fig. 12. Final spectrum $|a_{\vec{k}}|^2$. $t = 3378T_0$.

4.2. *The setup of the statistical model*

We augmented the numerical model used for solving the Hasselmann equation with a damping term in three different forms:

1. Pseudo-viscous high frequency damping (17) used in dynamical equations;
2. *WAM3* viscous term;
3. *WAM4* viscous term.

Two last viscous terms are the white-capping terms, describing energy dissipation by surface waves due to white-capping, as used in *WAM* wave forecasting models (in the *SWAN* model, the term used has different but similar tunable parameters), see [46]:

$$\gamma_{\vec{k}} = C_{\mathrm{ds}}\tilde{\omega}\frac{k}{\tilde{k}}\left((1-\delta)+\delta\frac{k}{\tilde{k}}\right)\left(\frac{\tilde{S}}{\tilde{S}_{\mathrm{pm}}}\right)^{p} \tag{24}$$

where k and ω are the wave number and frequency, tilde denotes mean value; C_{ds}, δ and p are tunable coefficients; $S = \tilde{k}\sqrt{H}$ is the overall steepness; $\tilde{S}_{\mathrm{pm}} = (3.02 \times 10^{-3})^{1/2}$ is the value of $\tilde{S}$ for the Pierson–Moscowitz spectrum (note

Author's personal copy

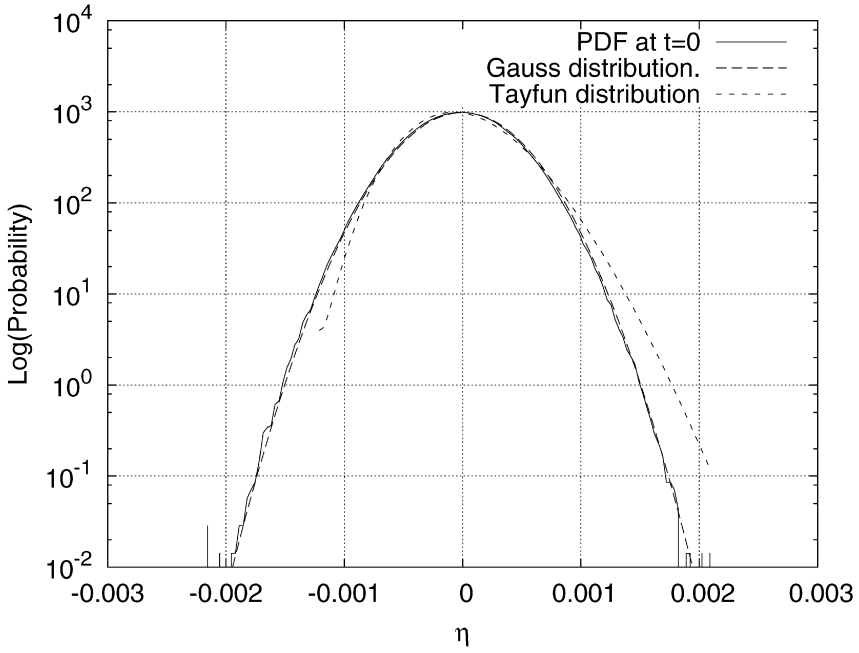

Fig. 13. PDF for the surface elevation η at the initial moment of time. $t = 0$.

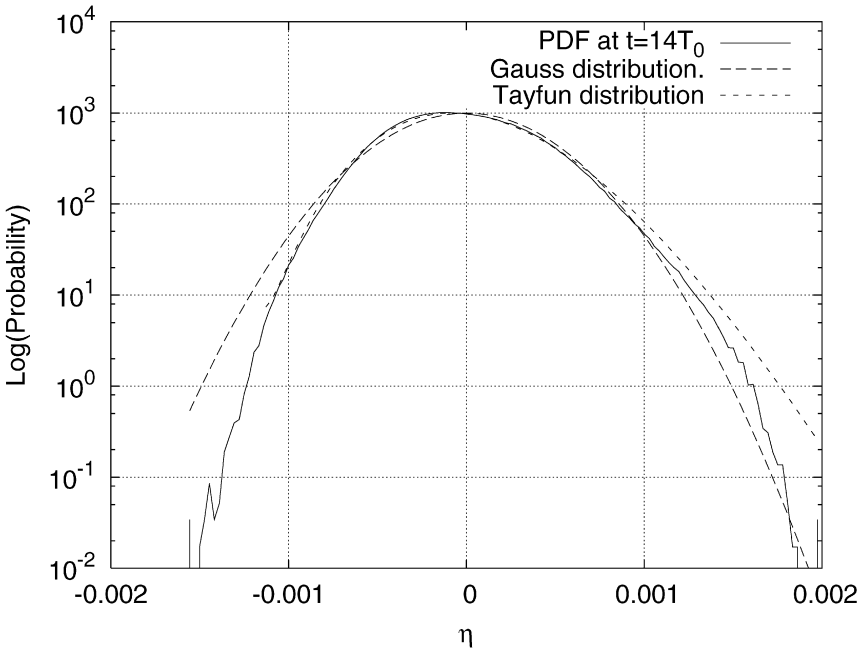

Fig. 14. PDF for the surface elevation η at the moment of maximum surface roughness. $t \simeq 14T_0$.

that the characteristic steepness is $\mu = \sqrt{2}S$). It is worth noting that according to [51] theoretical value of steepness for Pierson–Moscowitz spectrum is $S_{\mathrm{PM}} \simeq (4.57 \times 10^{-3})^{1.2}$. This gives us $\mu \simeq 0.095$.

The values of the tunable coefficients for the *WAM3* case are:

$$C_{\mathrm{ds}} = 2.36 \times 10^{-5}, \qquad \delta = 0, \qquad p = 4 \tag{25}$$

and for the *WAM4* case are:

$$C_{\mathrm{ds}} = 4.10 \times 10^{-5}, \qquad \delta = 0.5, \qquad p = 4. \tag{26}$$

Author's personal copy

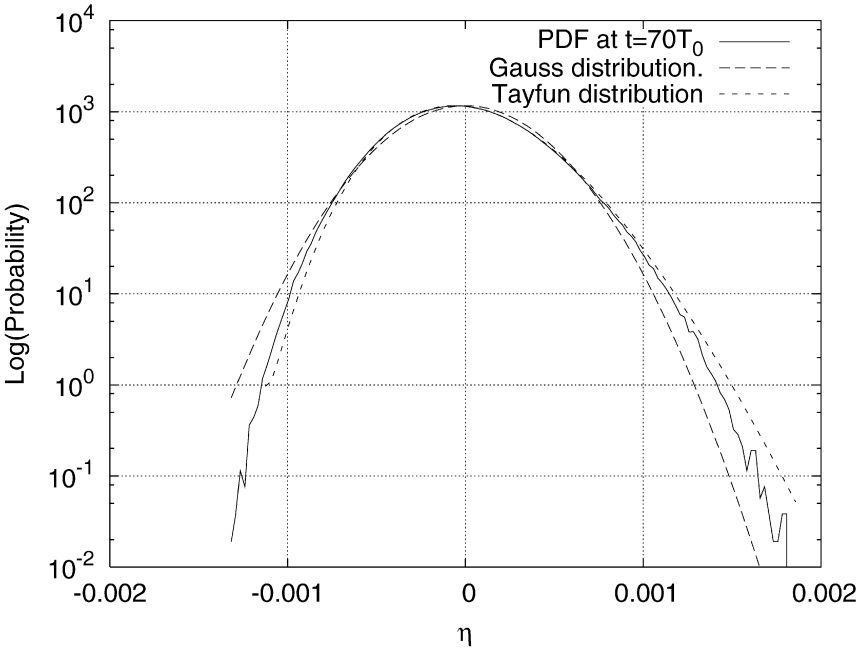

Fig. 15. PDF for the surface elevation η at an intermediate moment of time. $t \simeq 67.1T_0$.

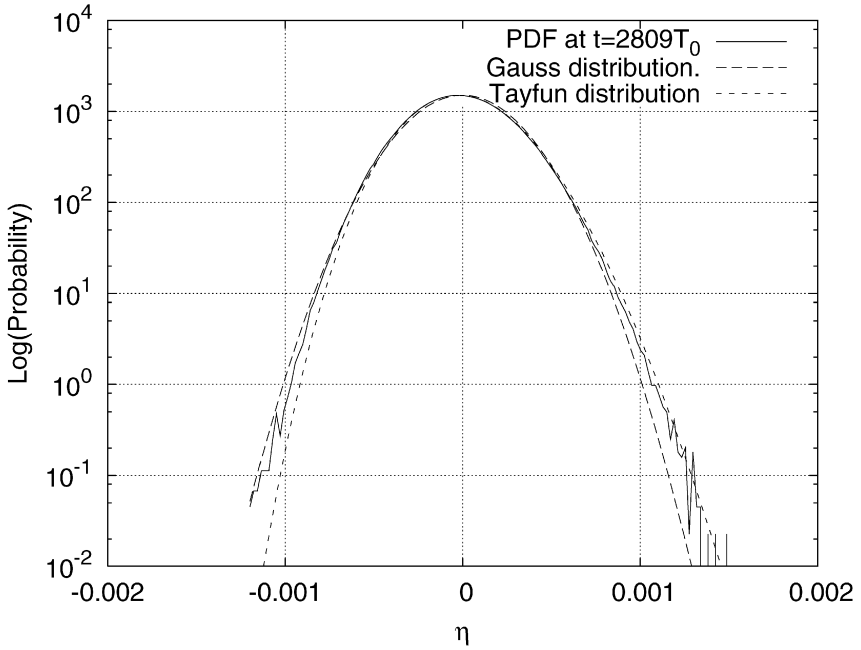

Fig. 16. PDF for the surface elevation η at the final moment of time. $t = 3378T_0$.

In all three cases, we used as initial data smoothed (filtered) spectra (see Fig. 19) obtained in the dynamical run at time $T_* = 3.65$ min $= 24.3 \simeq 67.1T_0$, which can be considered as the end moment of the first, rapid stage of spectral evolution.

The natural question arising in this point is: why do not we calculate the dynamical and Hasselmann model from the initial conditions (16) simultaneously?

There are good reasons for that:

As it was mentioned before, the time evolution of the initial conditions (16) in the presence of the damping term can be separated into two stages: a relatively fast total drop of energy at the beginning of the evolution and relatively slow succeeding total energy decrease as a function of time, see Fig. 8. We explain this phenomenon by the existence of an

Author's personal copy

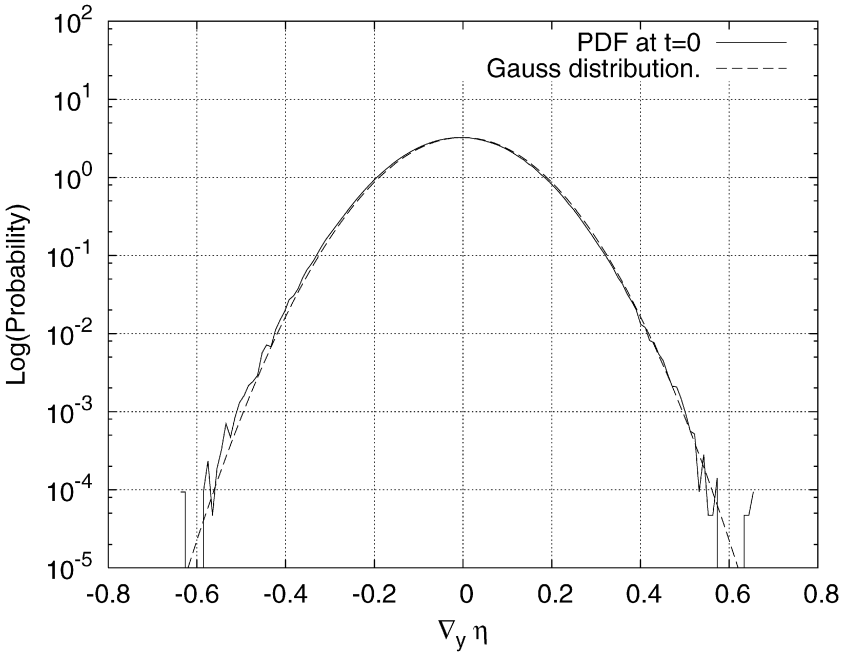

Fig. 17. PDF for $(\nabla\eta)_y$ at the initial moment of time. $t = 0$.

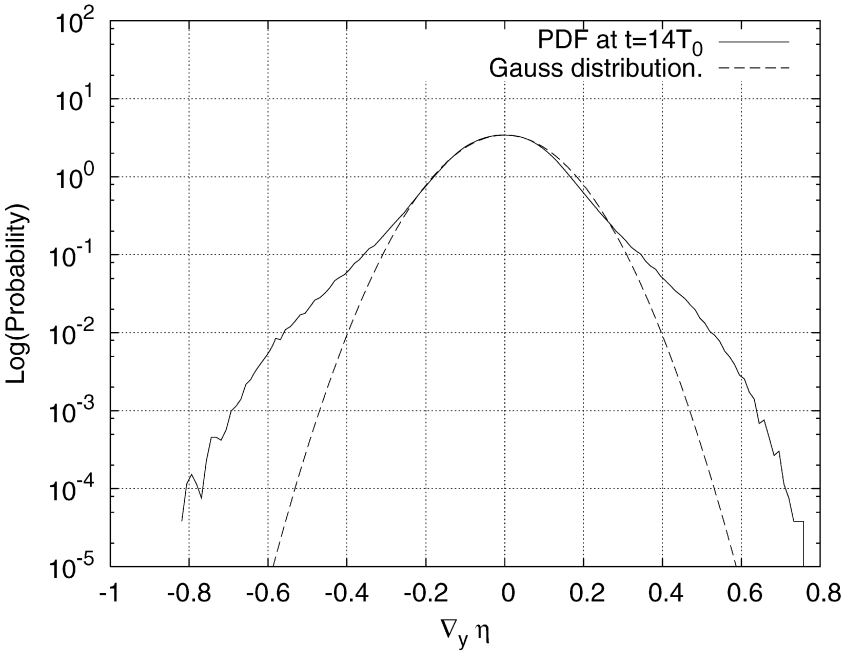

Fig. 18. PDF for $(\nabla\eta)_y$ at the moment of maximum surface roughness. $t \simeq 14T_0$.

effective channel of energy dissipation due to strong nonlinear effects, which can be associated with the white-capping we mentioned in the introduction.

We have started with relatively steep waves $\mu \simeq 0.167$. As we see, at that steepness white-capping is the leading effect. This fact is confirmed by numerous field and laboratory experiments. From the mathematical viewpoint, the white-capping is a formation of coherent structures – strongly correlated multiple harmonics. The spectral peak is initially situated in our experiments at $k \simeq 300$, while the edge of the damping area is $k_d \simeq 1024$. Hence, only the second and the third harmonic can develop, whereas higher harmonics are suppressed by strong dissipation. The formation of the second and the third harmonic is in any case enough to create an intensive non-Gaussian tail of the PDF for longitudinal gradients. This process is very fast. At the moment of time $T = 14T_0$ we see fully developed

Author's personal copy

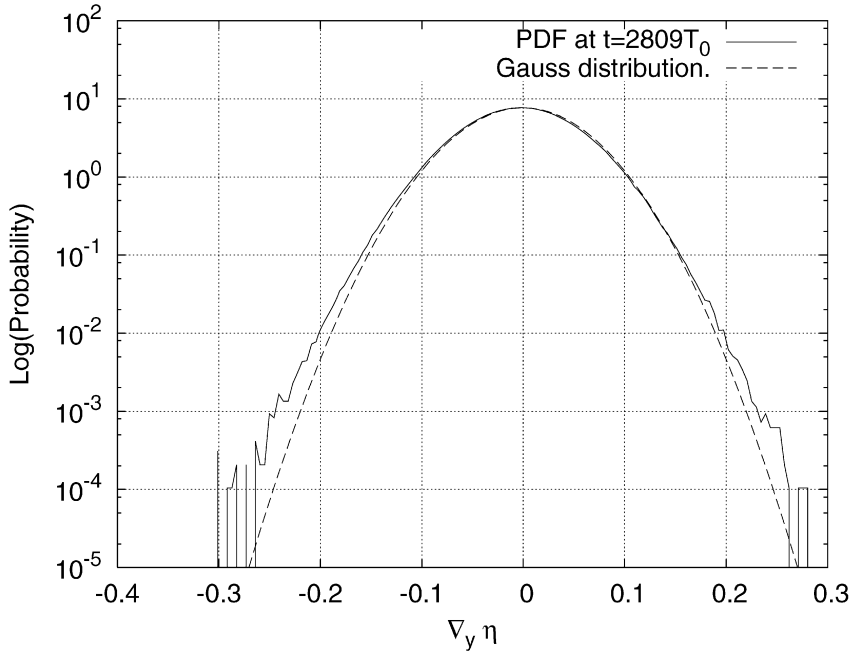

Fig. 19. PDF for $(\nabla\eta)_y$ at the final moment of time. $t = 3378T_0$.

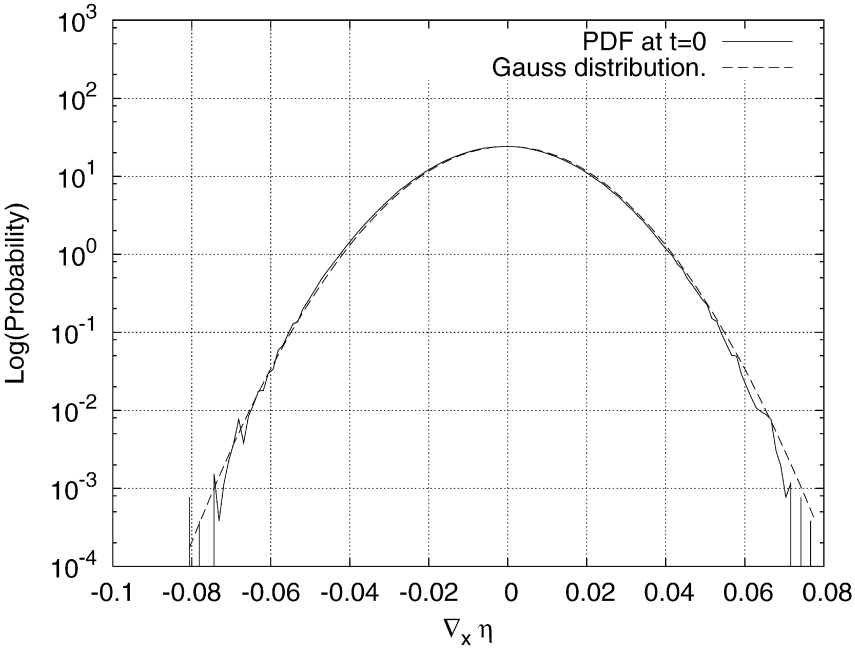

Fig. 20. PDF for $(\nabla\eta)_x$ at the initial moment of time. $t = 0$.

tails. Relatively sharp gradients mimic the formation of white caps. Certainly, the pure Hasselmann equation is not applicable on this early stage of spectral evolution, when energy intensively dissipates.

As the steepness decreases and spectral maximum of the swell downshifts, the efficiency of this mechanism of energy absorption decreases. When the steepness value drops down to $\mu \simeq 0.1$, at approximately $T \simeq 280T_0$, white-capping is negligibly small. Therefore, we decided to start comparing deterministic and statistical modeling at some intermediate moment of time $T \simeq 67.1T_0$.

Author's personal copy

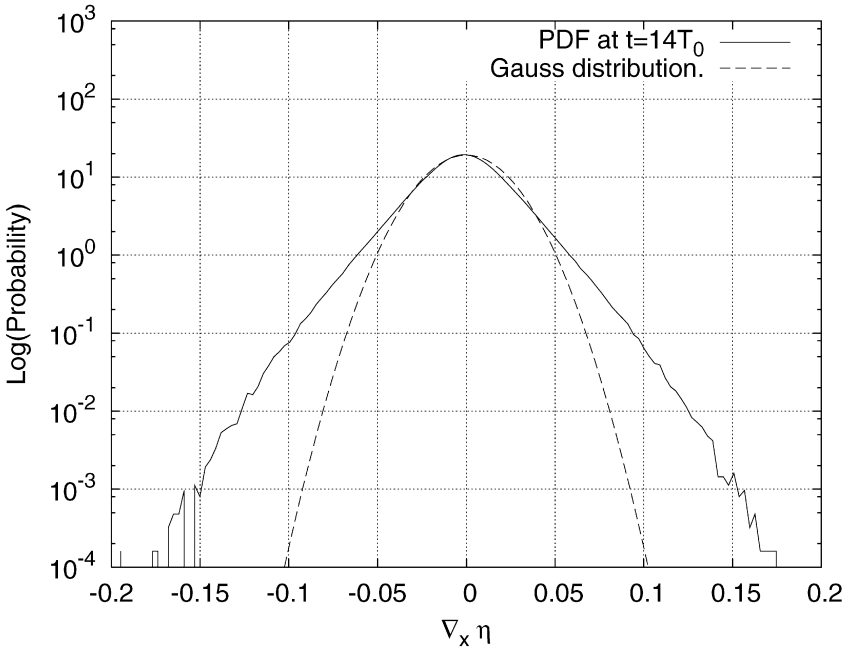

Fig. 21. PDF for $(\nabla\eta)_x$ at the moment of maximum surface roughness. $t \simeq 14T_0$.

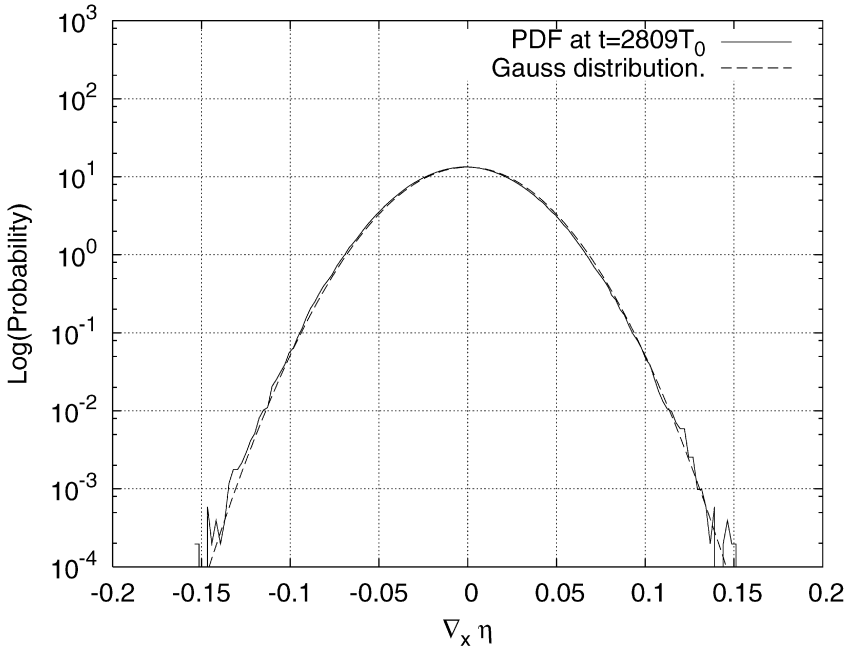

Fig. 22. PDF for $(\nabla\eta)_x$ at the final moment of time. $t = 3378T_0$.

5. A comparison of deterministic and statistical experiments

5.1. Statistical experiment with pseudo-viscous damping term

The first series of statistical experiments were performed with a pseudo-viscous damping term (17).

Figs. 7–10 show total wave action, total energy, mean wave slope and mean wave frequency as functions of time.

Fig. 31 shows the time evolution of angle-averaged wave action spectra as functions of frequency for dynamical and Hasselmann equations. We see a similar downshift of the spectral maximum both in dynamic and Hasselmann equations. The correspondence of the spectral maxima amplitudes is not good at all.

Author's personal copy

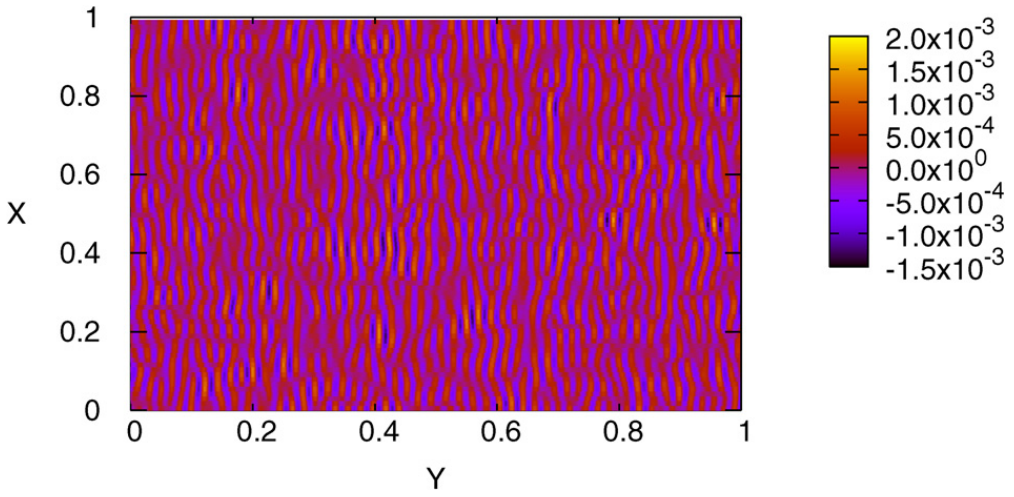

Fig. 23. Surface elevation at the initial moment of time. $t = 0$.

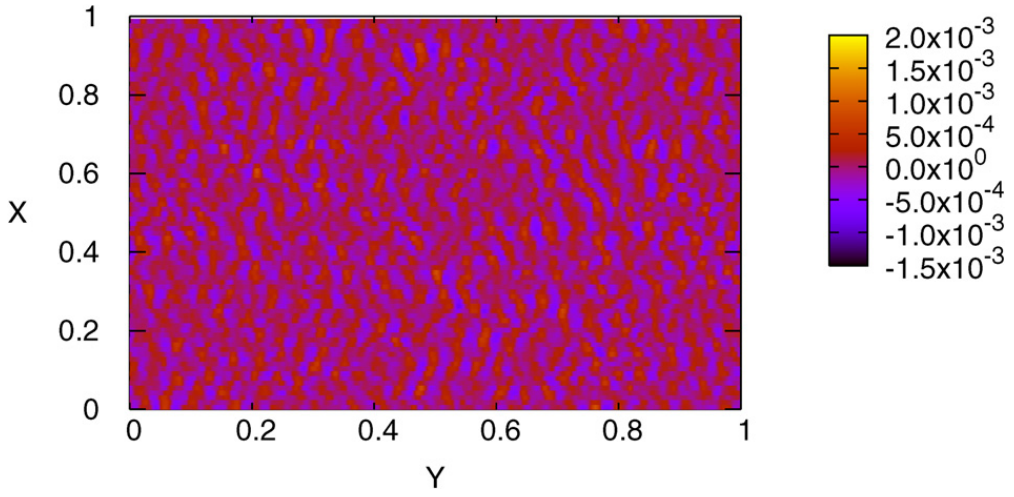

Fig. 24. Surface elevation at the final moment of time. $t = 3378T_0$.

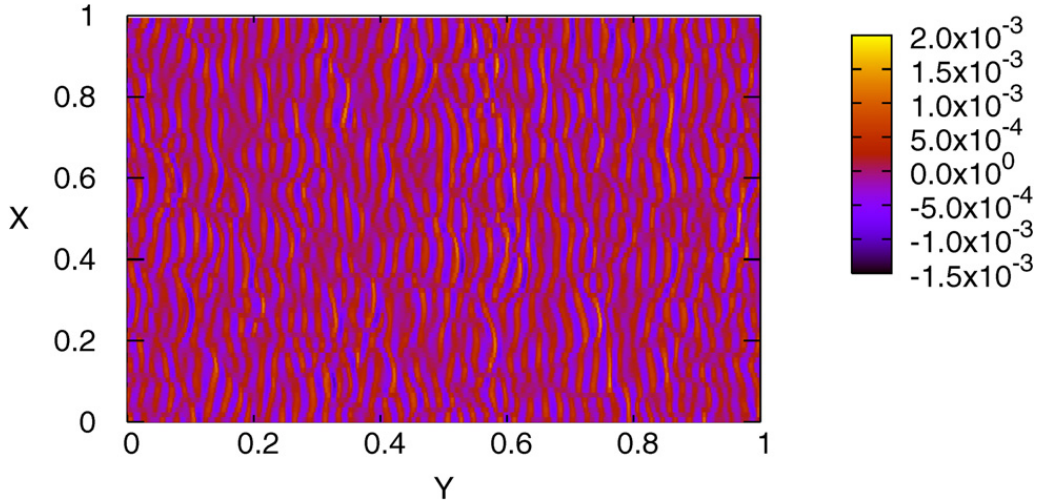

Fig. 25. Surface elevation at the moment of maximum surface roughness. $t \simeq 14T_0$. Gradients are more conspicuous.

Author's personal copy

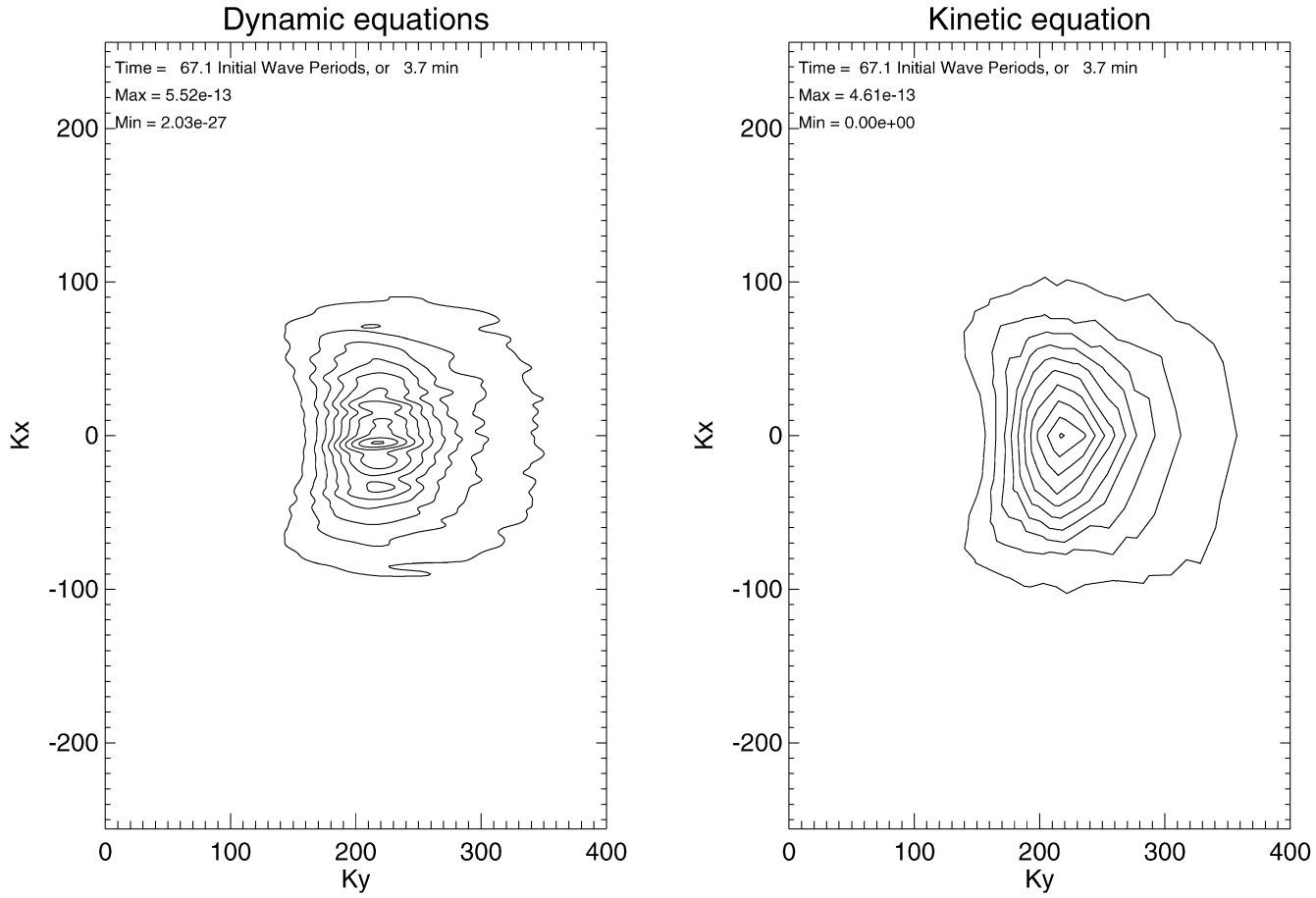

Fig. 26. Level lines of the dynamic (left) and the kinetic (right) spectra at $t = 67.1T_0$.

It is quite obvious that the influence of the artificial viscosity is not strong enough to give a correspondence of the two models.

5.2. Statistical experiments with a WAM3 damping term

The second series of statistical experiments were done with the *WAM3* damping term.

The temporal behavior of total wave action, energy and average wave slope (see Figs. 7–10) for the *WAM3* damping term is in better correspondence with the dynamical model than in the case of an artificial viscosity term. For the initial 50 min duration of the experiment we observe a decent correspondence between the dynamical and Hasselmann equations. For longer times, the *WAM3* model, however, deviates from the dynamical model significantly.

As in the artificial viscosity case, the angle-averaged wave action spectra exhibit, as function of frequency, a distinct down-shift of the spectral maxima both for the dynamical and the Hasselmann equations (see Fig. 32). The correspondence between time evolution of the amplitudes of the spectral maxima is also much better for a *WAM3* choice of damping than in the artificial viscosity case.

Presumably, the *WAM3* damping term underestimates the effects of real damping at the very beginning of the evolution (when the effects of white capping are relatively important), and overestimates them in the later stages of swell evolution.

5.3. Statistical experiments with the WAM4 damping term

The final third series of experiments were performed with a *WAM4* damping term.

Figs. 7–10 show the temporal evolution of the total wave action, total energy, mean wave slope and mean wave frequency, which are divergent in time in this case.

Author's personal copy

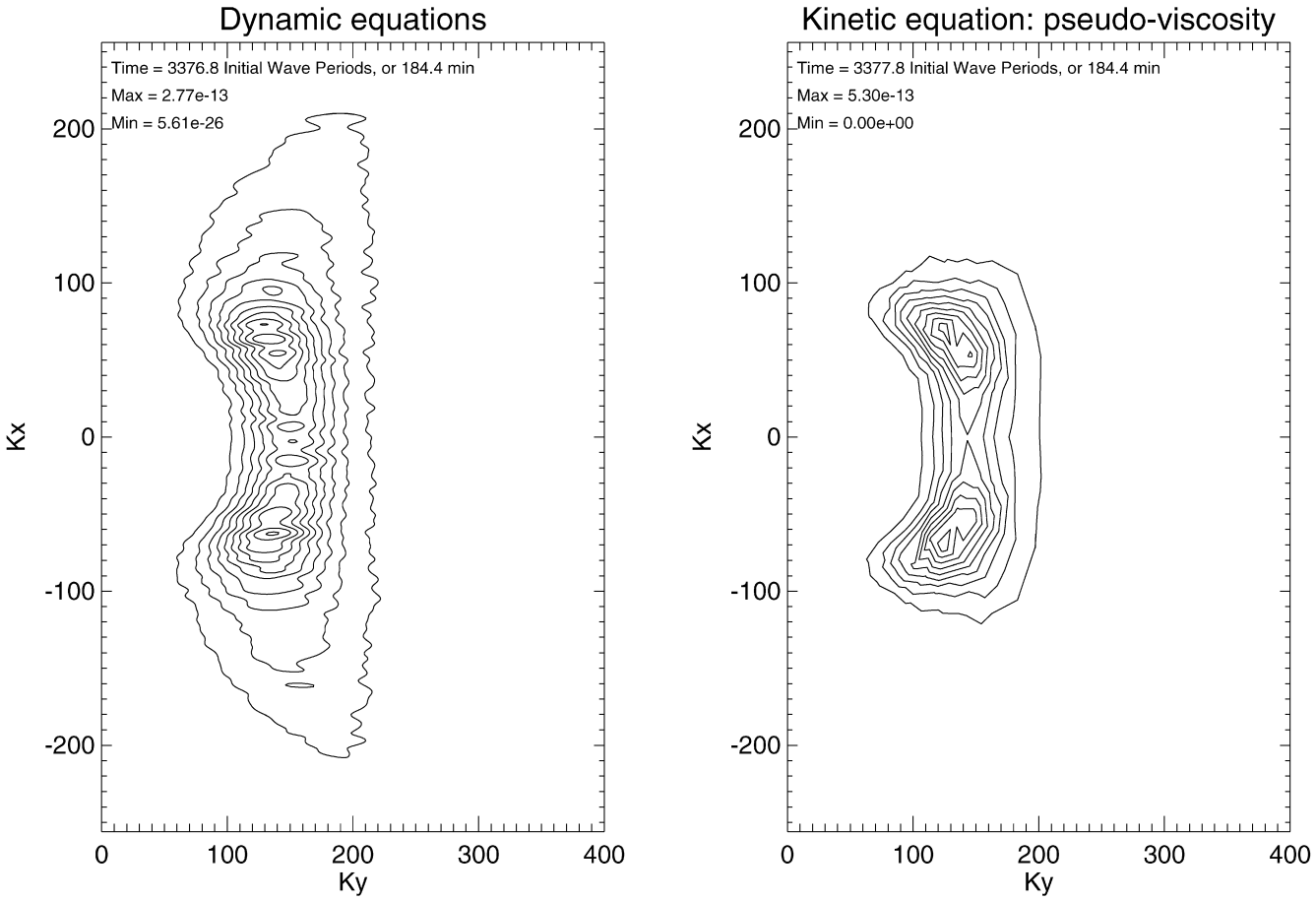

Fig. 27. Level lines of the dynamic (left) and the kinetic (right) spectra at $t = 3378.2T_0$.

Fig. 33 show the time evolution of the angle-averaged wave action spectra as functions of frequency for the dynamical and the Hasselmann equations. While we also observe a down-shift of the spectral maxima, as in the artificial viscosity and *WAM3* cases, the correspondence of the time evolution of the amplitudes of the spectral maxima is worse than in the *WAM3* case.

This observation is especially surprising in view of the fact that historically the *WAM4* damping term was invented as an improvement to the *WAM3* damping term. It is quite obvious that the *WAM4* damping is too strong for describing reality at all stages of the swell evolution.

6. Down-shift and angular spreading

The major process of time-evolution of the swell is frequency down-shift. During $T = 933T_0$ the mean frequency has decreased from $\omega_0 = 2$ to $\omega_1 = 0.6$. During the last stage of the process, the mean frequency slowly decays as

$$\langle\omega\rangle \sim t^{-0.067} \simeq t^{-1/15}. \tag{27}$$

The Hasselmann equation has a self-similar solution, describing the evolution of the swell $n(\vec{k}, t) \sim t^{4/11} F(\vec{k}/t^{2/11})$ (see [43,45]). For this solution

$$\langle\omega\rangle \sim t^{-1/11}. \tag{28}$$

The difference between (27) and (28) can be explained as follows. What we observed is not a self-similar behavior. Indeed, self-similarity presumes that the angular structure of the solution is constant in time. Meanwhile, we have observed intensive angular spreading of the initially narrow-in-angle, almost one-dimensional wave spectrum.

Level lines of the low-pass filtered dynamic and kinetic spectrum at the beginning of the simulation are presented on Fig. 26. There are ten isolines on every figure. The values of level at maximum and minimum isolines are shown on

Author's personal copy

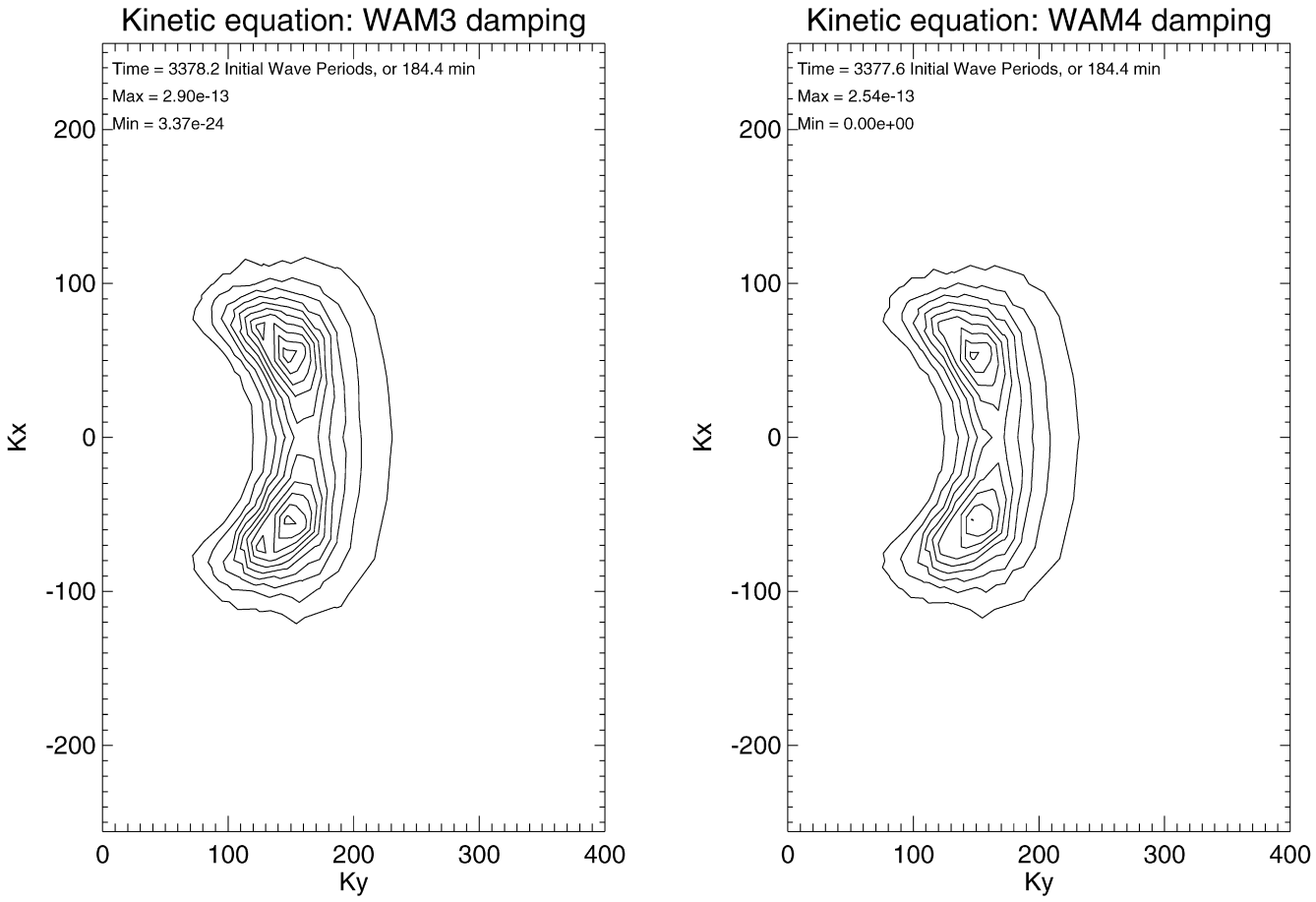

Fig. 28. (left) Level lines of the kinetic spectra in the *WAM3* (right) *WAM4* and damping cases at $t = 3378.2T_0$.

every picture. Level lines of the low-pass filtered dynamic and kinetic spectrum for three different damping terms at the end of the simulation are presented on Figs. 27–28. We observed the development of bimodality in both experiments. This is in accordance with field observations [53,54].

We observe good correspondence between the results of both experiments. A comparison of time-evolution of the mean angular spreading, calculated from action and energy spectra is shown on Figs. 29–30.

We see a growing divergence between dynamic and kinetic models. However, using the *WAM3* and the *WAM4* models leads to worse divergence. This is an additional argument against these variants of white-cap damping.

One can expect that the angular spreading will be arrested at later times, and the spectra will take on a universal self-similar shape.

7. Conclusion

1. Our numerical experiment shows that the Hasselmann equation without any additional terms is applicable for describing gravity wave turbulence in an infinite basin only if the nonlinearity is small enough. The average wave steepness $\mu = (E^2/N^2)\sqrt{2E}$ should be significantly less a certain critical level $\mu_0 = 0.095$. To describe the wave turbulence of a moderate steepness $0.095 < \mu < 0.15$, one should augment the Hasselmann equation by an additional term S_{diss} modeling dissipation due to white-capping. So far, there no any theory making it possible to find S_{diss} analytically. This is a great challenge for hydrodynamics. So far we can suggest that S_{diss} depends on steepness very sharply. Hence, the conjecture that white-capping is a threshold phenomenon formulated by Banner, Babanin, and Young [52] looks very plausible. We did not model overly steep waves, but we can conjecture that if $\mu > 0.15$, white capping is the leading nonlinear process and the weak-turbulent approach is not applicable at all.

Author's personal copy

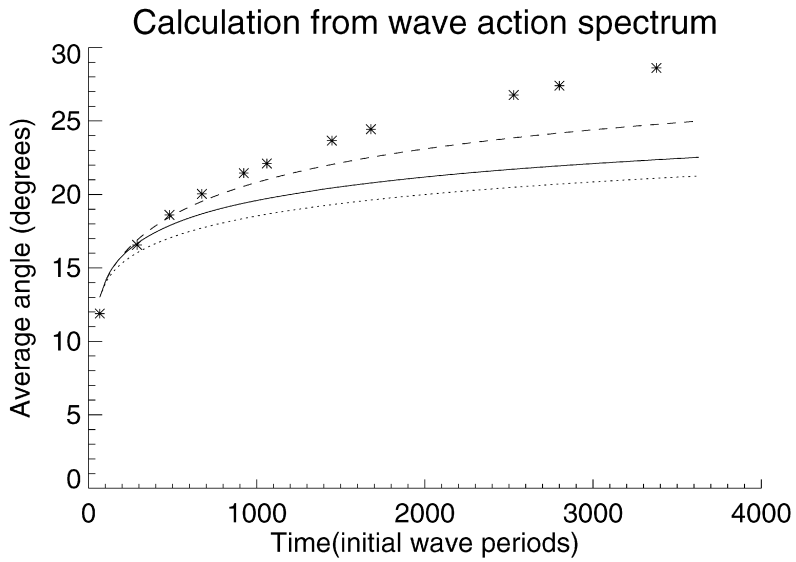

Fig. 29. Average angular spreading $(\int |\theta| n(\vec{k})\,\mathrm{d}\vec{k})/(\int n(\vec{k})\,\mathrm{d}\vec{k})$ as a function of time, calculated from wave action. The solid line corresponds to *WAM3*, the dotted line to *WAM4*, the dashed line to artificial viscosity, the stars to the dynamical equations.

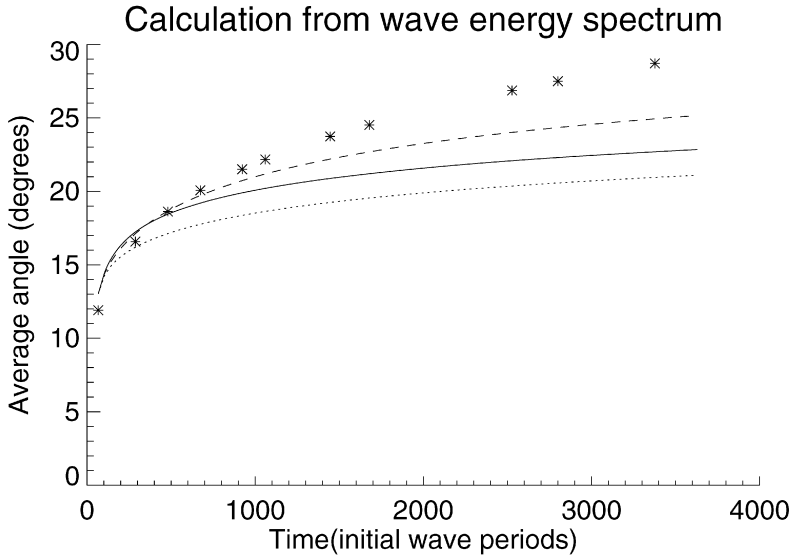

Fig. 30. Average angular spreading $(\int |\theta| \omega n(\vec{k})\,\mathrm{d}\vec{k})/(\int \omega n(\vec{k})\,\mathrm{d}\vec{k})$ as a function of time, calculated from wave energy. The solid line corresponds to *WAM3*, the dotted line to *WAM4*, the dashed line to artificial viscosity, the stars to the dynamical equations.

2. Our results are not a surprise for designers of operational models for wave forecasting. They understood the necessity of introducing extra dissipative terms into the models many years ago. It is a different story altogether that the models of S_{diss} routinely used in the WAM and WAVEWATCH models are too crude and do not grasp the most important feature of white-capping – its threshold nature. In our opinion, the existing models of S_{diss} overestimate dissipation at small values of steepness and underestimate it at large μ. Moreover, they overestimate dissipation in the area of the spectral peak and underestimate it in the spectral region of high wave numbers. We plan to offer our own form of S_{diss} extracted from our massive numerical simulation of the Euler equation, but this will take some time and toil.
3. We stress that we have solved a maximally idealized model. We did not take into account the interaction of the swell with atmosphere (see, for instance, [55,56]), the interaction with ocean currents, the deviation of the wave motion from potentiality as well as influence of turbulence in the surface–atmosphere boundary layer. In the future, we plan to establish contact with experimentalists to develop a more realistic model of swell propagation in the real ocean.

Author's personal copy

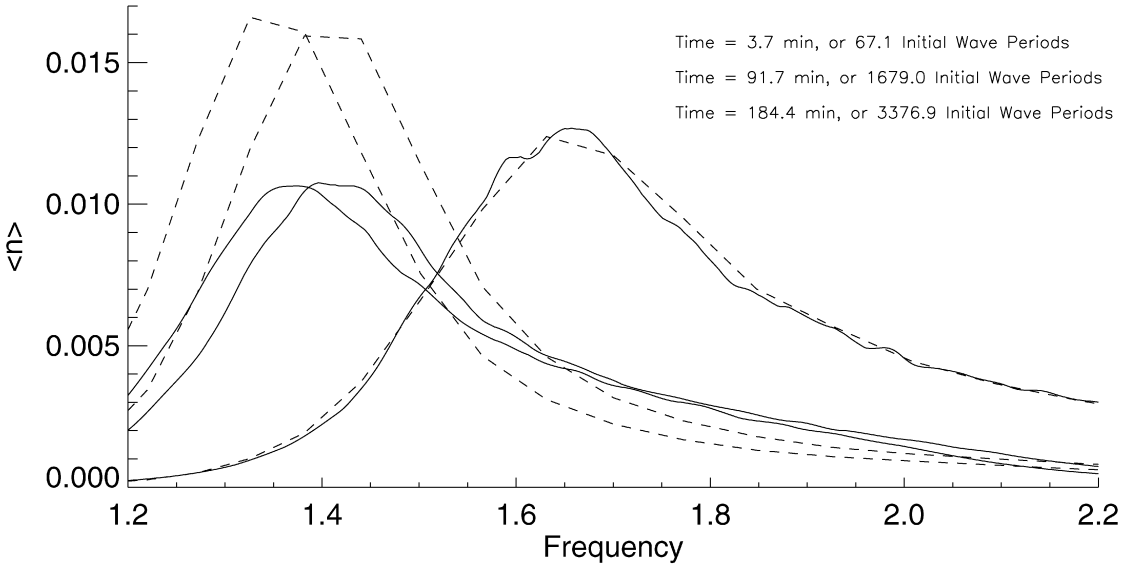

Fig. 31. Angle-averaged spectrum as a function of time for dynamical and Hasselmann equations for the artificial viscosity case.

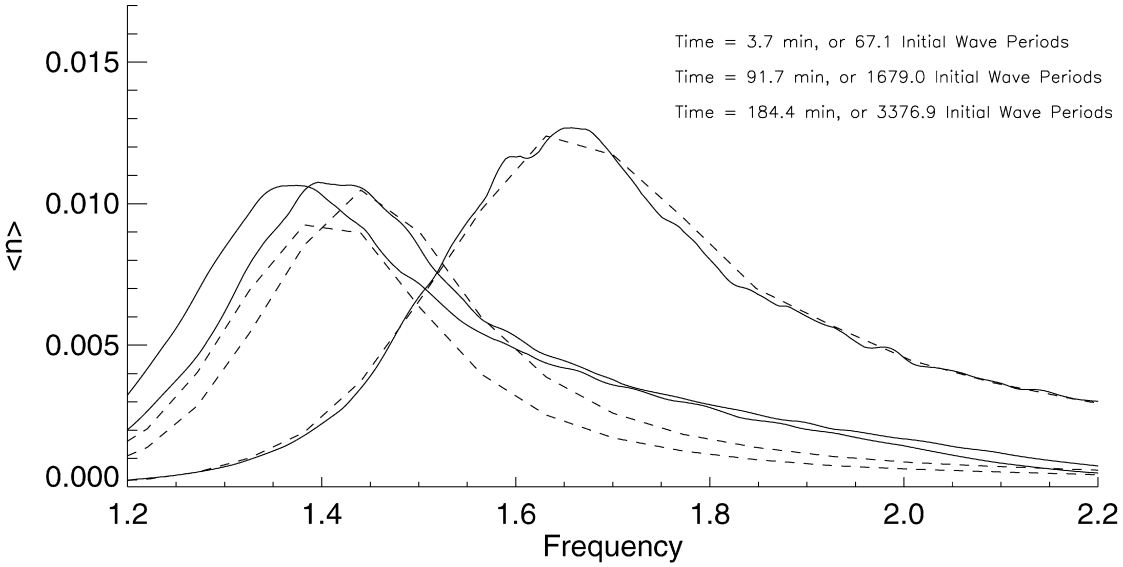

Fig. 32. Angle-averaged spectrum as a function of time for dynamical and Hasselmann equations a function of time for the *WAM3* case.

4. In one aspect our conclusions are very resolute. All existing experimental wave tanks cannot be used for modeling wave propagation in an open sea. The mesoscopic effects in wave tanks are too strong for reasonable values of steepness. This pertains only to the modeling of the kinetics of the energy containing region in the vicinity of spectral peak. The rear faces of spectral distributions, spectral tails, can be successfully modeled. This was demonstrated by Toba in his classical work [29]. Toba observed the Zakharov–Filonenko spectrum $I_\omega \sim \omega^{-4}$ in a wave tank of moderate size. In our opinion, this conclusion is very important. Some authors, trying to find a universal law of fetch dependence of mean energy and mean frequency, have put together data collected in the ocean and in experimental tanks. This mixed data can hardly be compared with any self-sufficient theory. This question is discussed in detail in [57].

Another conclusion is more pessimistic. The results of numerical experiments show that it is very difficult to reproduce real ocean conditions in a laboratory wave tank. Even a size of 200×200 meters is insufficient to model the ocean due to the discreteness of the wave number grid.

Author's personal copy

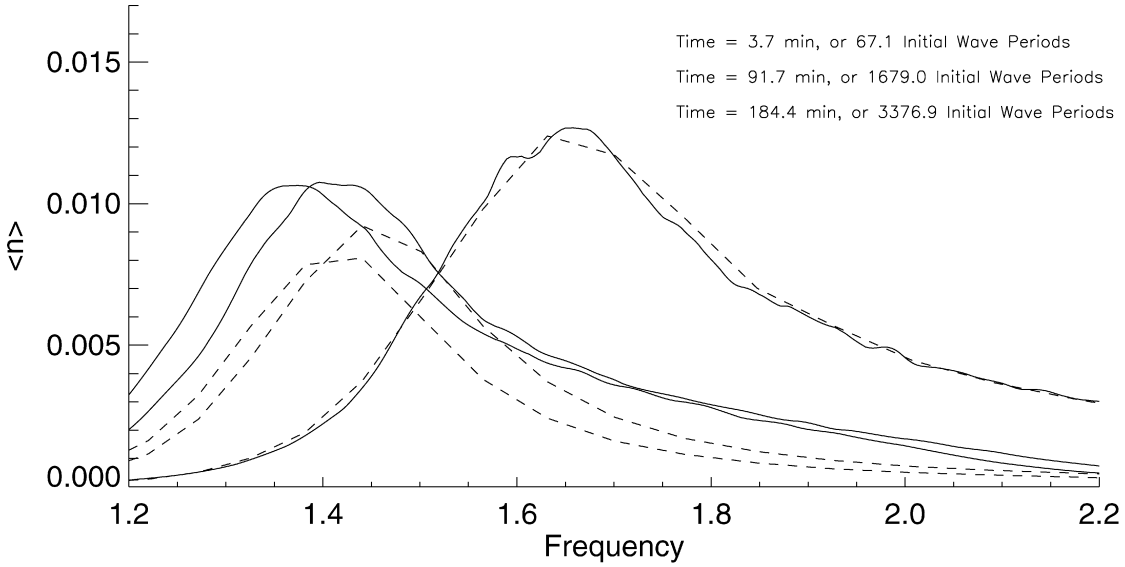

Fig. 33. Angle-averaged spectrum as a function of time for dynamical and Hasselmann equations a function of time for the *WAM4* case.

Acknowledgements

This work was supported by ONR grant N00014-06-C-0130, US Army Corps of Engineers Grant W912HZ-04-P-0172, RFBR grant 06-01-00665-a, the Programme "Nonlinear dynamics and solitons" from the RAS Presidium and "Leading Scientific Schools of Russia" grant NSh-7550.2006.2, also by and by NSF Grant NDMS0072803. We use this opportunity to gratefully acknowledge the support of these foundations.

A.O. Korotkevich was also supported by Russian President grant for young scientist MK-1055.2005.2.

The authors would also like to thank the creators of the open-source fast Fourier transform library FFTW [58] for this fast, portable and completely free piece of software.

Appendix A. From dynamical equations to Hasselmann equation

The standard setup for numerical simulation of the dynamical equations (4) implies a $2\pi \times 2\pi$ domain in real space and gravity acceleration $g = 1$. The use of a domain size equal 2π is convenient because in this case the wave numbers are integers.

Contrary to the dynamical equations, the kinetic equation (12) is formulated in terms of real physical variables and it is necessary to describe the transformation from the dynamical variables into to the physical ones.

Eq. (4) are invariant with respect to a stretching transformation from the dynamical to the real variables:

$$\eta_{\vec{r}} = \alpha \eta'_{\vec{r}'}, \qquad \vec{k} = \frac{1}{\alpha}\vec{k}', \qquad \vec{r} = \alpha \vec{r}', \qquad g = \nu g', \tag{A.1}$$

$$t = \sqrt{\alpha/\nu}\, t', \qquad L_x = \alpha L'_x, \qquad L_y = \alpha L'_y, \tag{A.2}$$

where prime denotes variables corresponding to dynamical equations.

In our simulation, we used a stretching coefficient of $\alpha = 800.00$, which allows us to reformulate the statement of the problem in terms of real physics: we considered 5026 m $\times$ 5026 m periodic boundary conditions domain of statistically uniform ocean with the same resolution in both directions and characteristic wave length of the initial condition at around 22 m. In oceanographic terms, this statement corresponds to a duration-limited experiment.

References

[1] L.W. Nordheim, Proc. R. Soc. A 119 (1928) 689.
[2] R. Peierls, Ann. Phys. (Leipzig) 3 (1929) 1055.
[3] V.E. Zakharov, G. Falkovich, V.S. Lvov, Kolmogorov Spectra of Turbulence I, Springer-Verlag, Berlin, 1992.

Author's personal copy

[4] K. Hasselmann, J. Fluid Mech. 12 (48) (1962) 1.
[5] V.E. Zakharov, N.N. Filonenko, Dokl. Akad. Nauk SSSR 160 (1966) 1292.
[6] A.N. Pushkarev, V.E. Zakharov, Phys. Rev. Lett. 76 (18) (1996) 3320.
[7] A.N. Pushkarev, European J. Mech. B/Fluids 18 (3) (1999) 345.
[8] A.N. Pushkarev, V.E. Zakharov, Physica D 135 (2000) 98.
[9] M. Tanaka, J. Fluid Mech. 444 (2001) 199.
[10] M. Onorato, A.R. Osborne, M. Serio, et al., Phys. Rev. Lett. 89 (2002) 14–144501, nlin.CD/0201017.
[11] K.B. Dysthe, K. Trulsen, H.E. Krogstad, H. Socquet-Juglard, J. Fluid Mech. 478 (2003) 1–10.
[12] A.I. Dyachenko, A.O. Korotkevich, V.E. Zakharov, JETP Lett. 77 (10) (2003) 546, physics/0308101.
[13] A.I. Dyachenko, A.O. Korotkevich, V.E. Zakharov, Phys. Rev. Lett. 92 (13) (2004) 134501, physics/0308099.
[14] N. Yokoyama, J. Fluid Mech. 501 (2004) 169.
[15] V.E. Zakharov, A.O. Korotkevich, A.N. Pushkarev, A.I. Dyachenko, JETP Lett. 82 (8) (2005) 487, physics/0508155.
[16] H. Socquet-Juglard, K. Dysthe, K. Trulsen, H.E. Krogstad, J. Liu, J. Fluid Mech. 542 (2005) 195.
[17] Yu. Lvov, S.V. Nazarenko, B. Pokorni, Physica D 218 (1) (2006) 24, math-ph/0507054.
[18] S.V. Nazarenko, J. Stat. Mech. (2006) L02002, nlin.CD/0510054.
[19] F. Dias, A.I. Dyachenko, V.E. Zakharov, (2007), arXiv: 0704.3352.
[20] S.Yu. Annenkov, V.I. Shrira, Phys. Rev. Lett. 96 (2006) 204501.
[21] A.I. Dyachenko, A.C. Newell, A. Pushkarev, V.E. Zakharov, Physica D 57 (1992) 96.
[22] A.O. Korotkevich, PhD thesis, L.D. Landau Institute for Theoretical Physics RAS, Moscow, Russia, 2003.
[23] A.I. Dyachenko, A.O. Korotkevich, V.E. Zakharov, JETP Lett. 77 (9) (2003) 477, physics/0308100.
[24] V.E. Zakharov, J. Appl. Mech. Tech. Phys. 2 (1968) 190.
[25] V.E. Zakharov, Eur. J. Mech. B/Fluids 18 (1999) 327.
[26] A. Kolmogorov, Dokl. Akad. Nauk SSSR 30 (1941) 9;
A. Kolmogorov, Proc. R. Soc. London A 434 (1991) 9.
[27] V.E. Zakharov, PhD thesis, Budker Institute for Nuclear Physics, Novosibirsk, USSR, 1967.
[28] V.E. Zakharov, M.M. Zaslavskii, Izv. Atm. Ocean. Phys. 18 (1982) 747.
[29] Y. Toba, J. Oceanogr. Soc. Jpn. 29 (1973) 209.
[30] M.A. Donelan, J. Hamilton, W.H. Hui, Phil. Trans. R. Soc. London, A 315 (1985) 509.
[31] P.A. Hwang, et al., J. Phys. Oceanogr. 30 (2000) 2753.
[32] A.I. Dyachenko, V.E. Zakharov, Phys. Lett. A 190 (1994) 144.
[33] A. Tayfun, J. Geophys. Res. 85 (1980) 1548.
[34] S. Hasselmann, K. Hasselmann, T.P. Barnett, J. Phys. Oceanogr. 15 (1985) 1378.
[35] J.C. Dungey, W.H. Hui, Proc. R. Soc. A 368 (1985) 239.
[36] A. Masuda, J. Phys. Oceanogr. 10 (1981) 2082.
[37] A. Masuda, in: O.M. Phillips, K. Hasselmann (Eds.), Waves Dynamics and Radio Probing of the Ocean Surface, Plenum Press, New York, 1986.
[38] I.V. Lavrenov, Mathematical Modeling of Wind Waves at Non-Uniform Ocean, Gidrometeoizdat, St. Petersburg, 1998.
[39] V.G. Polnikov, Wave Motion 1008 (2001) 1.
[40] D.J. Webb, Deep-Sea Res. 25 (1978) 279.
[41] D. Resio, B. Tracy, Theory and calculation of the nonlinear energy transfer between sea waves in deep water, Hydraulics Laboratory, US Army Engineer Waterways Experiment Station, WIS Report 11, 1982.
[42] D. Resio, W. Perrie, J. Fluid Mech. 223 (1991) 603.
[43] A. Pushkarev, D. Resio, V.E. Zakharov, Physica D 184 (2003) 29.
[44] A. Pushkarev, V.E. Zakharov, in: 6th International Workshop on Wave Hindcasting and Forecasting, November 6–10, Monterey, California, USA, Meteorological Service of Canada, 2000.
[45] S.I. Badulin, A. Pushkarev, D. Resio, V.E. Zakharov, Nonlinear Processes in Geophysics, 2005.
[46] SWAN Cycle III user manual, http://fluidmechanics.tudelft.nl/swan/index.htm.
[47] V.E. Zakharov, P. Guyenne, F. Dias, Physica D 573 (2001) 152–153.
[48] F. Dias, A. Pushkarev, V.E. Zakharov, Physics Reports 398 (2004) 1.
[49] F. Dias, P. Guyenne, A. Pushkarev, V.E. Zakharov, Preprint N2000-4, Centre de Mathematiques et del leur Appl., E.N.S de CACHAN, 1, 2000.
[50] P. Guyenne, V.E. Zakharov, F. Dias, Contemp. Math. 283 (2001) 107.
[51] I.R. Young, Wind Generated Ocean Waves, Elsevier, Amsterdam, 1999.
[52] M.L. Banner, A.V. Babanin, I.R. Young, J. Phys. Oceanogr. 30 (12) (2000) 3145.
[53] K.C. Ewans, J. Phys. Oceanogr. 28 (3) (1998) 195.
[54] D.W. Wang, P.A. Hwang, J. Phys. Oceanogr. 31 (5) (2001) 1200.
[55] W.M. Drennan, H.C. Graber, M.A. Donelan, J. Phys. Oceanogr. 29 (8) (1999) 1853.
[56] A.A. Grachev, C.W. Fairall, J.E. Hare, J.B. Edsond, S.D. Miller, J. Phys. Oceanogr. 33 (11) (2003) 2408.
[57] S.I. Badulin, A.V. Babanin, V.E. Zakharov, D. Resion, J. Fluid Mech. (2007), in press.
[58] M. Frigo, S.G. Johnson, Proc. IEEE 93 (2) (2005) 216, http://fftw.org.